Inverse Electromagnetic Scattering Models for Sea Ice

K. M. Golden, D. Borup, *Member, IEEE*, M. Cheney, E. Cherkaeva, M. S. Dawson, *Member, IEEE*, Kung-Hau Ding, A. K. Fung, *Fellow, IEEE*, D. Isaacson, *Member, IEEE*, S. A. Johnson, Arthur K. Jordan, *Life Fellow, IEEE*, Jin Au Kong, *Fellow, IEEE*, Ronald Kwok, *Member, IEEE*, Son V. Nghiem, *Member, IEEE*, Robert G. Onstott, *Member, IEEE*, J. Sylvester, D. P. Winebrenner, *Senior Member, IEEE*, and I. H. H. Zabel

Abstract—Inverse scattering algorithms for reconstructing the physical properties of sea ice from scattered electromagnetic field data are presented. The development of these algorithms has advanced the theory of remote sensing, particularly in the microwave region, and has the potential to form the basis for a new generation of techniques for recovering sea ice properties, such as ice thickness, a parameter of geophysical and climatological importance. Moreover, the analysis underlying the algorithms has led to significant advances in the mathematical theory of inverse problems. In particular, the principal results include the following.

1) Inverse algorithms for reconstructing the complex permittivity in the Helmholtz equation in one and higher dimensions, based on layer stripping and nonlinear optimization, have been obtained and successfully applied to a (lossless) laboratory system. In one dimension, causality has been imposed to obtain stability of the solution and layer thicknesses can be obtained from the recovered dielectric profile, or directly from the reflection data through a nonlinear generalization of the Paley–Wiener theorem in Fourier analysis.

2) When the wavelength is much larger than the microstructural scale, the above algorithms reconstruct a profile of the effective complex permittivity of the sea ice, a composite of pure ice with random brine and air inclusions. A theory of inverse homogenization has been developed, which in this quasistatic regime, further inverts the reconstructed permittivities for microstructural information beyond the resolution of the wave. Rigorous bounds on brine volume and inclusion separation for a given value of the effective complex permittivity have been obtained as well as an accurate algorithm for reconstructing the brine volume from a set of values.

3) Inverse algorithms designed to recover sea ice thickness have been developed. A coupled radiative transfer—thermodynamic sea ice inverse model has accurately reconstructed the growth of a thin, artificial sea ice sheet from time-series electromagnetic scattering data. Inversions for sea ice thickness have also been obtained through the application of neural networks to an analytic wave theory model, a reflectivity inversion scheme, and the use of proxy indicators. The role of neural networks in sea ice classification is also considered.

It is anticipated that the broad-ranging advances in inverse scattering theory presented here may find application to closely related problems, such as medical imaging, geophysical exploration, and nondestructive testing of materials as well as generating new techniques for remotely reconstructing sea ice parameters.

Index Terms—Dielectric materials, electromagnetic scattering by random media, electromagnetic scattering inverse problems, nonhomogeneous media, remote sensing, sea ice, snow.

K. M. Golden and E. Cherkaeva are with the Department of Mathematics, University of Utah, Salt Lake City, UT 84112 USA (e-mail: golden@math.utah.edu).

D. Borup and S. A. Johnson are with the Department of Bioengineering, University of Utah, Salt Lake City, UT 84112 USA.

M. Cheney and D. Isaacson are with the Department of Mathematical Sciences, Rensselaer Polytechnic Institute, Troy, NY 12180 USA.

M. S. Dawson and A. K. Fung are with the Electrical Engineering Department, University of Texas, Arlington, TX 76019 USA.

K.-H. Ding and J. A. Kong are with the Department of Electrical Engineering, Massachusetts Institute of Technology, Cambridge, MA 02139 USA.

A. K. Jordan is with the Remote Sensing Division, Naval Research Laboratory, Washington, DC 20375 USA.

R. Kwok and S. V. Nghiem are with the Jet Propulsion Laboratory, California Institute of Technology, Pasadena, CA 91109 USA.

R. G. Onstott is with the Environmental Research Institute of Michigan, Ann Arbor, MI 48113-4001 USA.

J. Sylvester is with the Department of Mathematics, University of Washington, Seattle, WA 98195 USA.

D. P. Winebrenner is with the Applied Physics Laboratory, University of Washington, Seattle, WA 98195 USA.

I. H. H. Zabel was with the Byrd Polar Research Center, Ohio State University, Columbus, OH 43210-1002 USA. She is now with Lincoln Laboratory, Massachusetts Institute of Technology, Lexington, MA 02173-9108 USA.

Publisher Item Identifier S 0196-2892(98)06382-7.

I. INTRODUCTION

A. Sea Ice Remote Sensing and Electromagnetic Inverse Scattering

IN SEA ice remote sensing, observations of electromagnetic fields scattered or emitted by sea ice are used to characterize the physical state and dynamics of the sea ice pack. Large-scale information obtained in this way is important for our understanding of global climate and the world ocean system and for conducting operations in the polar regions. Realizing the potential of remote-sensing techniques depends on the development of theoretical, as well as practical, methods of inverting observed electromagnetic data to obtain information

on sea ice. While there is a substantial body of existing work on forward modeling of electromagnetic scattering and propagation in sea ice [107], nevertheless, the application of forward theory to the inversion of sea ice parameters has been somewhat empirical and *ad hoc*. In the forward, or direct, problem, the electromagnetic scattering properties of a multilayer random medium, such as the sea ice system, are calculated based on knowledge of its local complex permittivity $\epsilon(\mathbf{x})$, which takes a wide range of values in the principal constituents of the sea ice system: pure ice, air, brine, and sea water. In the corresponding inverse problem, we wish to obtain information about $\epsilon(\mathbf{x})$ and the sea ice characteristics from knowledge of the far-field scattering properties. Electromagnetic inverse scattering theory [13], [22], [48], [54] has been developed to address the fundamental problem of reconstructing the parameters of a complex medium from scattering data.

Here we report on the first systematic effort to use such ideas to develop inverse scattering algorithms for reconstructing sea ice physical properties from data on scattered electromagnetic fields and to compare the reconstructions with experimental data. This effort has led to significant advances in inverse scattering theory itself, as well as the successful recovery in some circumstances of important sea ice parameters, such as ice thickness, brine volume, and geometry. The recovery of sea ice thickness for the case of thin ice, as is considered here, is particularly significant. Heat transfer in winter from the ocean to the atmosphere can be one or two orders of magnitude greater through thin ice cover than through thick multiyear ice [67]. Thickness information on thin ice is thus essential in heat budget calculations for the polar regions, as well as in other considerations discussed below. The inverse models considered here, which yield such reconstructions, are based on the forward models presented in [41], and this paper is a continuation of [41]. More background on the interaction of electromagnetic waves with sea ice, remote sensing, and the Office of Naval Research Sea Ice Electromagnetics Accelerated Research Initiative (ARI), which led to the present results, can be found.

As discussed in [41], there is a vast literature on the forward electromagnetic scattering problem for general inhomogeneous media extending back to the 1800's [75], [97]. In contrast, work on the inverse scattering problem has only recently progressed from a collection of *ad hoc* techniques with little rigorous mathematical basis, to a blossoming field of intense activity, with the beginnings of a mathematical foundation [22]. Much of the early work on inverse scattering took place in the context of quantum mechanics [48], motivated by Rutheford's efforts [84] to reveal the internal structure of atoms by firing energetic particles at them. This work culminated in the discovery of the atomic nucleus and prompted the development of the quantum theory and Schrödinger's wave equation. Inverse scattering theory for the Schrödinger equation became a subject of paramount importance. Eventually, Born [6] showed that if the scattering interaction was sufficiently weak, there was a simple relationship between the scattered field and the scattering potential. The Born approximation was able to verify Rutherford's classical solution in the high-energy limit and provided the first linearized solution to

the inverse scattering problem. More recently, much of the activity has been driven by the central role that electromagnetic and acoustic inverse scattering play in such technologically important problems as radar, sonar, geophysical exploration, medical imaging and tomography, nondestructive testing, and remote sensing [22], [48]. From a theoretical standpoint, inverse problems are difficult because not only are they nonlinear, but they are also "ill-posed." In 1923, Hadamard [45] introduced the concept of a *well-posed* problem, originating from the philosophy that a mathematical model of a physical problem should have the properties of existence, uniqueness, and stability of the solution [54]. If one of these properties fails to hold, the problem is said to be *ill-posed*. While the forward electromagnetic scattering problem is well-posed, the corresponding inverse problem is ill-posed, which is a general feature of many inverse problems. In particular, given enough scattering data, often the existence and uniqueness of solutions to inverse problems can be forced by enlarging or reducing the solution space. However, in the inverse scattering problem, large changes in the medium can correspond to very small changes in the measured data. Because of this, reconstruction algorithms tend to be unstable, and much effort in this field revolves around obtaining algorithms that are stable, as we shall see below.

The main techniques for dealing with inverse problems [22], [31], [54], [78] include the following: 1) optimization, 2) linearization, and 3) continuation methods, such as layer stripping and successive linearization. Optimization methods, in which parameters describing the reconstructed medium are optimized to minimize the error between predicted and measured scattering data, have the advantage of being robust and broadly applicable; their disadvantage is that they tend to be computationally intensive. Linearization is the method of choice for a problem that is "close" in some sense to a known one. For example, the weak scattering, or high-energy situation necessary for the Born approximation, is "close" to the case with no scatterer. Continuation methods exhibit different advantages and disadvantages. Layer-stripping methods involve, in one way or another, solving for the index of refraction at progressively increasing depths in the reflecting medium. In this manner, the medium is mathematically stripped away, layer by layer, and the medium parameters are found in the process. Some forms of layer stripping are fast but unstable. Other continuation methods are more stable but tend to be computationally intensive.

An issue in inverse scattering theory that is particularly relevant to the reconstruction of sea ice features is resolution. The local complex permittivity $\epsilon(\mathbf{x})$ of the sea ice system exhibits variations over many length scales. For example, $\epsilon(\mathbf{x})$ varies dramatically on a submillimeter scale as $\mathbf{x}$ moves from pure ice into a brine inclusion. When the wavelength is much larger than the microstructural scale, the wave cannot resolve the fine structure and it "sees" an effective, homogenized medium. In the context of inverse scattering theory, the reconstructed permittivity will then be the effective complex permittivity ϵ^* for sea ice, which is considered at length in [41]. This reconstructed effective permittivity will itself likely vary on a larger scale throughout the ice sheet according to,

for example, variations in brine volume with depth. In the case of sea ice, it is quite desirable to be able to further invert the reconstructed effective complex permittivity data to obtain detailed information on the nature of the brine and air microstructure. Such characteristics are closely connected to the fluid and thermal transport properties of the sea ice as well as the distinction between different ice types, such as first year and multiyear, or frazil and columnar. In [41], we dealt with the forward homogenization problem of how the microstructure determines ϵ^*. Here we develop a theory of *inverse homogenization*, in which data on homogenized coefficients of a composite medium, such as the effective complex permittivity ϵ^* of sea ice, are inverted to obtain information on the microstructure, or the local complex permittivity $\epsilon(\mathbf{x})$. In this way, inverse scattering theory can be used in conjunction with inverse homogenization theory to recover information on fine details well beyond the resolution of the wave. Our theory applies at present to the quasistatic regime discussed in detail in [41], in which scattering from individual brine inclusions is neglected. The quasistatic assumption, which is certainly not valid throughout the microwave region, nevertheless provides a good approximation for the lower frequency part, such as at C-band.

B. Summary of Main Results

In [41], we noted that the main goals of the ARI were to improve our understanding of how the physical properties of sea ice determine its electromagnetic behavior and, in turn, to use this knowledge to develop and test inverse algorithms for recovering sea ice parameters from observed electromagnetic data. In this paper, we show how the forward scattering models considered in [41] have been used to develop such inverse algorithms. From an inverse modeling perspective, our principal results include the following.

1) Stable inverse algorithms for the Helmholtz equation in one dimension that have accurately reconstructed real permittivity profiles (neglecting dissipation) from reflection data. The algorithms are based on a new, causally stabilized layer-stripping technique, arising from a nonlinear generalization of the Plancherel equality in Fourier analysis, and nonlinear optimization of parameters via the Ribere–Polack algorithm. Layer thicknesses can be deduced either from the reconstructed permittivity profile or directly from the reflection data via an analog of the Paley–Wiener theorem in Fourier analysis. A layer-stripping algorithm to recover the complex permittivity for the Helmholtz equation in higher dimensions (including dissipation) has also been developed. Through a geometrical optics-based technique, the algorithm has accurately reconstructed surface permittivity, yet at present is unstable for reconstruction at depth.

2) Stable inverse algorithms that have accurately reconstructed thickness information on thin sea ice from scattering data. The algorithms employ a variety of methods: inversion of parameters from time-series scattering data by the Levenberg–Marquardt nonlinear least-squares optimization algorithm coupled with a radiative

transfer—thermodynamic sea ice model, neural network inversion of an analytic wave theory model, and reflectivity inversion. The use of proxy indicators of sea ice thickness has also been explored.

3) A rigorous theory of inverse homogenization in the quasistatic regime, which has produced an accurate algorithm for reconstructing the brine volume of sea ice from measurements of the effective complex permittivity. The algorithm is based on inversion of a series of bounds on the complex permittivity of sea ice, which in turn yields bounds on microstructural parameters, such as brine volume and inclusion separation.

The paper is organized as follows. In Section II, we present rigorous inverse scattering theory for the Helmholtz equation and the algorithms that reconstruct permittivity profiles. In Section III, we consider rigorous inverse homogenization theory that further inverts these reconstructed permittivities for microstructural information. Inverse algorithms designed to recover sea ice thickness are presented in Section IV, and in Section V, we consider a sea ice classification algorithm.

The main results are summarized as follows. In Section II-A, we first consider the Helmholtz (2.2) with an index of refraction $n(z) = \sqrt{\epsilon(z)}$ (neglecting dissipation), varying only in the vertical or depth variable z, with $n(z)$ constant for $z > 0$ (air). It has long been known that the reflection coefficient $R(\omega)$, where ω is angular frequency, uniquely determines $n(z)$. However, all previous layer-stripping algorithms for continuous or discrete $n(z)$ rely on trace formulas, and (with one major exception [14]) these formulas are not stable enough to permit rigorous analysis of convergence and stability. By basing the technique instead on the nonlinear generalization of the Plancherel theorem discussed in [41], the first mathematically complete formulation of a stable layer-stripping algorithm for a continuous medium $n(z)$ has been obtained [94]. Indeed, both convergence of the algorithm and well-posedness of the (forward and) inverse scattering problem have been proven. Moreover, the stability is achieved by imposing causality, at every depth, on the estimate of the depth-varying reflection coefficient. The resulting method is surprisingly stable under noisy perturbations, with reasonable reconstructions, even with significant noise in the data. The deep connection of the approach in [94] to Fourier analysis has also led to a nonlinear analog of the Paley–Wiener theorem [110]. This classical theorem relates the growth of the transform in the complex frequency domain to the width of the support of the function in the real-time (or spatial) domain. The nonlinear analog of this theorem, which requires only the modulus, but not the phase of the reflection data, yields the thickness of the reflecting layer, albeit in a depth coordinate scaled by the travel time through the layer, so that an estimate of the effective permittivity of the medium is required to obtain the actual thickness. In the case of sea ice, even a rough guess of the effective permittivity provides physical thickness estimates with accuracies of about 10%.

Subsequently, in Section II-B, we consider an optimization approach to inverting for $n(z)$ in the one-dimensional (1-D) Helmholtz equation, neglecting dissipation, developed

by Borup and Johnson (which is published here for the first time). The medium is assumed to consist of N layers, and the forward scattering model used for comparison to the scattering data is provided by the exact scattering solution for an N layer slab [71]. The least-squares functional measuring the error between data calculated from the model for a given discrete permittivity profile and the actual scattering data is minimized using the Ribere–Polack algorithm [81]. Optimal permittivity parameters describing $n(z)$ are then obtained. The method has been accurately compared with data taken on a layered medium consisting of slabs of drywall and polystyrene foam on top of sand. The causally stabilized layer-stripping algorithm in Section II-A has also been applied with apparent success to this same data set.

A layer-stripping algorithm that reconstructs the complex permittivity $\epsilon(\mathbf{x}) = \epsilon_r/\epsilon_0 + i\sigma/(\omega\epsilon_0)$, where ϵ_r is the (real) permittivity, ϵ_0 is the permittivity of free space, and σ is the conductivity in a perturbed dissipative half space [16], is presented in Section II-C. The algorithm involves two steps, first finding the medium parameters on the surface and then synthesizing the data on a subsurface. A method, based on geometrical optics, which reconstructs the surface parameters by taking into account the change in pulse shape when the pulse is reflected from a dissipative medium, is developed. In particular, geometrical optics predicts that an incident delta function will reflect as a delta function plus a series of terms with increasing smoothness. The coefficient of the second-order term can be used to obtain the conductivity. To synthesize subsurface data, the scattering data can be used to obtain the Dirichlet-to-Neumann map, and then this map can be used to obtain a Riccati equation for the subsurface data, which is then solved iteratively, beginning with the surface parameters constructed first. The reconstruction of surface parameters gives good results on simulated stepped-frequency radar data, but the layer-stripping algorithm is at present unstable.

In Section III, the question of how to recover the microstructure of a composite material, such as sea ice, from measurements of its effective complex permittivity ϵ^* in the quasistatic regime is rigorously addressed. In [41], we presented a series of forward bounds on ϵ^*, which grow tighter as more microstructural information is known [36], [39], [85]. These bounds are based on a Stieltjes integral representation for ϵ^* involving a spectral measure μ, which depends only on the geometry of the microstructure. A theorem is presented which establishes that, if the values of ϵ^* are known along some arc in the complex plane, which could be a small interval along the real axis, the measure μ can be uniquely recovered [18]. Knowing μ yields all the statistical properties of the microstructure, and from the point of view of effective properties, completely determines the microstructure. However, as may be expected from our discussion of inverse problems, this problem is ill-posed and requires regularization for stability of the solution. Nevertheless, for a single-known value of ϵ^*, the forward bounds can be inverted to obtain rigorous bounds on microstructural parameters, such as brine volume [19] and inclusion separation [77], which is related to connectedness of the brine phase.

For many known values of ϵ^*, these inverse bounds yield an accurate algorithm for recovering microstructural parameters. This algorithm has been applied to C-band measurements of the effective complex permittivity of laboratory grown sea ice, and it has accurately reconstructed brine volume data. Information on brine volume and connectedness is important in understanding the transport properties of sea ice, which undergo a fundamental transition at the critical brine volume fraction $p_c \approx 5\%$ for percolation [40]. This transition in the transport properties plays a significant role in a number of processes in the geophysics [1], [62] and biology [33] of sea ice, particularly in the Antarctic. Inversion for such detailed microstructural information offers the prospect of remotely monitoring these processes.

The thickness distribution of sea ice plays a key role in the geophysics of the polar regions [102]. Together with the ice extent, it defines the response of sea ice to climatic changes, and together with ice velocity, it defines the mass flux of sea ice. By itself, the thickness distribution is a quantity of central importance in ocean-atmosphere heat exchange. It is particularly important to understand the details of the distribution for thin ice, such as in leads, which permit large heat fluxes. Net heat flux through thin ice occupying a relatively small aereal fraction is significantly larger than through thick, multiyear ice [67], [68]. While recovery of the sea ice thickness distribution is of clear significance, obtaining such information on a large scale has remained a challenging problem. Submarine sonar profiling has provided an accurate characterization of the thickness distribution over some areas of the Arctic basin, yet this method has serious limitations of spatial coverage and temporal resolution [102]. Remote sensing can overcome these limitations, but the success of this approach has been somewhat limited. Analysis of active and passive microwave signatures of sea ice, and how they depend on thickness, has shed some light on this problem [43], [46], [102], [108]. However, the basic question of how to directly reconstruct the thickness of a complex, dynamic medium, such as sea ice, from electromagnetic scattering data has remained, from an inverse theoretic point of view, largely unaddressed. In Section IV, we present inverse scattering algorithms that can reconstruct sea ice thickness for the important thin ice case. Along with the methods discussed in Section II, namely, the nonlinear Paley–Wiener theorem and recovery from the dielectric profile, these algorithms provide the first concerted effort at directly attacking the thickness reconstruction problem.

First, in Section IV-A, an algorithm, based on radiative transfer theory, to invert for ice thickness from time-series scattering data, is presented [86], [87]. The algorithm uses a parametric estimation approach in which the radiative transfer equation is used as the direct scattering model to calculate the backscattering signatures from the sea ice. The Levenberg–Marquardt method [65] is employed to retrieve ice thickness iteratively. Additional information provided by the saline ice thermodynamics is used to constrain the electromagnetic inverse problem to achieve a reasonably accurate reconstruction. The algorithm is applied to reconstruct the growth of a sheet of thin saline ice by using C-band (with

center frequency 5 GHz) polarimetric radar measurements taken sequentially in time, during the United States Cold Regions Research and Engineering Laboratory, Hanover, NH, 1993 Experiment (CRRELEX'93). Agreement with the data is obtained.

In Section IV-B, the use of neural networks to invert for the thickness of young sea ice with multifrequency polarimetric microwave data is demonstrated. The approach is to retrieve the ice thickness by using the analytic wave theory model [41], [72] to train the neural network to match measured data in the selection of the ice thickness. The multilayer random medium model used allows for the inclusion of surface and volume scattering, contributions from a slush layer, and roughness at the interfaces. There are several types of neural networks, but here, the multilayer perceptron is used, with a modified backpropagation algorithm to improve the convergence rate and accuracy [49]. Interrelations among physical parameters governed by sea ice physics under typical Arctic winter environmental conditions are utilized to restrict the solution space to avoid extraneous solutions and shorten the required computation time. The algorithm accurately retrieves thin ice thicknesses from polarimetric synthetic aperture radar (SAR) data taken in the Beaufort Sea, Antarctica.

In Section IV-C, the relations between ice thickness and both the coherent and incoherent reflectivity properties of a layer of saline ice over saline water are considered. It is shown that a new incoherent reflectivity along with the standard coherent reflectivity are needed to explain reflectivity measurements. For thicker ice, the coherency between the transmitted and reflected field is lost and the reflectivities of VV- and HH-polarizations become incoherent. The transition to this type of behavior takes place when the ice thickness is between one and two wavelengths, and it is found that thickness can be inverted directly from reflectivity measurements when the thickness is over one wavelength.

Proxy indicators of ice thickness are discussed in Section IV-D. A remotely sensed proxy indicator is a characteristic, physical property, suite of physical properties that is tied to ice thickness, or some other characteristic, and that has a measurable electromagnetic signature. In this section, the use of surface roughness, dielectric properties, and surface temperature are explored as proxy indicators for sea ice thickness.

Finally, in Section V, we consider a classification scheme for sea ice types based on a special neural network known as the fast-learning neural network [28], [63]. The scheme is illustrated with a specific example using passive radiometric data from the spaceborne SSM/I platform. After the original image is classified using an unsupervised method and the identity of each class is known, the final classified image can be used as pseudoground truth for a supervised neural network classification scheme. Representative data from each class and an associated class identification tag are dumped to a file and used to train the neural network. The trained network classifier can then be used for batch processing satellite or aircraft data. Eventually, it is hoped that such practical methods can be combined with the rather theoretical results and algorithms presented earlier in this paper, to systematize the inversion of

important sea ice parameters of geophysical, climatological, and operational significance.

II. INVERSE SCATTERING THEORY FOR THE HELMHOLTZ EQUATION

In this section, we formulate the inverse scattering problem for the inhomogeneous Helmholtz equation with local complex permittivity $\epsilon(\mathbf{x})$ and present algorithms that reconstruct $\epsilon(\mathbf{x})$, or partial information about $\epsilon(\mathbf{x})$, such as layer thicknesses or surface permittivities, from far-field scattering data. This section is a continuation of [41, Section II]. For completeness, we include here the basic setup and definitions.

The sea ice inverse scattering problem can be modeled as a half-space problem in $\mathbf{R}^d$, where measurements are made in the upper half-space, which is homogeneous and nondissipative, while the lower half-space is inhomogeneous and dissipative. We consider an electromagnetic wave of a particular frequency in such a medium (assumed nonmagnetic), whose time-harmonic electric field is given by $\mathbf{E}(\mathbf{x}, t) = \mathbf{E}(\mathbf{x})e^{-i\omega t}, \mathbf{x} \in \mathbf{R}^d, \mathbf{x} = (x_1, x_2, x_3)$ in $d = 3$, $t \in \mathbf{R}$, with $\omega = 2\pi f$ and f the frequency in hertz. The relative complex permittivity $\epsilon(\mathbf{x})$ of the medium, assumed locally isotropic, is given by $\epsilon = \epsilon_r/\epsilon_0 + i\sigma/(\omega\epsilon_0)$, as above. In the upper half space occupied by air $\epsilon = 1$, with zero imaginary part. In the lower half space occupied by sea ice, snow, and sea water, $\epsilon(\mathbf{x})$ takes a wide range of values in the constituents. The electric field $\mathbf{E}(\mathbf{x}, t)$ satisfies Maxwell's equations, or the vector wave equation derived from them. For simplicity, we assume that the medium is unchanging in the x_2 direction, and we consider the transverse electric (TE) polarization case with $\mathbf{E} = (0, E_2, 0)$ in the x_2 direction. Under the time-harmonic assumption, $u = E_2$ satisfies the Helmholtz equation with spatially varying complex permittivity

$$\nabla^2 u(\mathbf{x}) + k^2 \epsilon(\mathbf{x}) u(\mathbf{x}) = 0 \qquad (2.1)$$

where k is the free-space wavenumber $k = \omega\sqrt{\mu_0\epsilon_0} = \omega/c$, μ_0 is the magnetic permeability of free space, c is the velocity of light in free space, and the Laplacian ∇^2 is two-dimensional (2-D) in the x_1 and x_3 variables. It will be useful in (2.1) to write $k^2\epsilon = k^2 n^2 + ikm$, where $n = \sqrt{\epsilon_r/\epsilon_0}$ is the index of refraction and $m = \sigma\sqrt{\mu_0/\epsilon_0}$.

The inverse scattering problem for (2.1) consists of determining $\epsilon(\mathbf{x})$ from the far-field pattern u_∞ or, more precisely, from knowledge of the scattering operator that maps incident fields to scattered fields. Existence and uniqueness of solutions to the inverse scattering problem for (2.1) in various settings are discussed in [11], [12], [16], [21], [22], [54], [56], and [64]. Due to the often layered nature of the sea ice system, we are particularly interested in (2.1) in the 1-D case with depth variable $z = x_3$. The inverse scattering problem in this case, including dissipation, with $\epsilon = n^2 + im/k$, has been studied by a number of authors. In particular, the papers [11], [12], [56], and [64] show that time-domain backscattered data from a single incident plane wave is not enough data to determine both n^2 and m if n^2 and m are smooth. In this case, both reflected and transmitted data are needed. If, on the other hand, n^2 and m have a jump discontinuity at the

bottom, backscattered data do suffice to determine both. This is because the reflected data from the discontinuity at the bottom provides information that is similar to transmission data. In the following section, we consider a new type of layer-stripping algorithm for solving the inverse scattering problem for the Helmholtz equation in one dimension.

A. Inversion by Causally Stabilized Layer Stripping in One Dimension

The term layer stripping applies to a variety of inverse scattering methods that involve the use of reflection data to solve for the index of refraction at increasing depths in the reflecting medium (i.e., at progressively greater distances from the level at which the observations are made). A "reflection coefficient" at each depth is computed, which in physical terms, is that reflection coefficient that would exist if we were to replace all of the material above that depth with material having a constant refractive index equal in value to that of the actual refractive index value at that depth. If we take into account no physics other than that inherent in the Helmholtz equation, errors in refractive index estimates at shallow depths lead to unphysical estimates of the reflection coefficient and refractive index deeper in the medium.

The essential element in causally stabilized layer stripping is that we *require*, at every depth the estimate of the depth-varying reflection coefficient correspond to a causal impulse response for the remaining reflecting material. It turns out that a simple enforcement for frequency-domain reflection coefficients is sufficient to guarantee stability of our inverse solution in the presence of noise in the data. Moreover, work to establish the method has lead to two theorems that generalize theorems in standard Fourier analysis to the nonlinear inverse problem, that is, to the situation in which multiple reflections in the reflecting medium are significant. One of these theorems turns out to be useful in its own right as means of estimating the travel time thickness of a reflecting layer (and, if appropriate ancillary information about the permittivity is available, the physical thickness of the layer as well). These results have been established rigorously for the case of wave propagation in a system governed by the Helmholtz equation without loss and without discontinuities in dielectric properties. Computational evidence shows, however, that simple modifications of the same results provide usefully approximate solutions in problems, including both dielectric jumps and loss typical of sea ice.

In the following, we first briefly recall the forward scattering problem from [41] and our analog, for the reflection problem, of the Plancherel equality in linear Fourier analysis. We then outline our causally stabilized layer-stripping algorithm, followed by our analog of the classical Paley–Wiener theorem, which relates the travel-time thickness of a reflecting layer with finite physical thickness to a Fourier transform of a nonlinear function of the reflection data. We demonstrate the utility of these results using laboratory data from a system somewhat simpler than sea ice.

The Helmholtz equation governing the time-harmonic wave field u in one dimension, assuming sources only at infinity

and neglecting dissipation, is

$$\frac{d^2u}{dz^2} + k^2 n^2(z)u = 0. \qquad (2.2)$$

We assume that n differs from one only on the interval $(-\infty, 0)$, and that $\frac{d}{dz}\frac{1}{\sqrt{n}}$ is square-integrable on that interval. The auxiliary equation for the wave field $v(x) \equiv u(z(x))$ as a function of the depth variable $x(z) \equiv \int_0^z n(\tau)\,d\tau$ is

$$v'' + \alpha v' + k^2 v = 0 \qquad (2.3)$$

where $\alpha(x) \equiv \frac{1}{\gamma(x)}\frac{d\gamma}{dx}$ and $\gamma(x) \equiv n(z(x))$. For $x > 0$, $v(x, k)$ may be written in the form

$$v(x, k) = \frac{1}{T(k)}[e^{-ikx} + R(k)e^{ikx}] \qquad (2.4)$$

which uniquely defines the reflection coefficient $R(k)$. The additional requirements that the time-domain impulse response of the reflecting medium be real and causal, i.e., that there can be no response prior to excitation, force $R(-k) = \overline{R(k)}$, for k on the real axis, where the overbar denotes complex conjugation and $R(k)$ to extend analytically to the upper half of the complex k-plane. Equation (2.4) represents the wave field above the reflecting medium in terms of reflected and incident plane waves. Inside the reflecting medium, we define a "depth-dependent reflection coefficient"

$$r(x, k) \equiv \frac{1 - \eta(x, k)}{1 + \eta(x, k)} \qquad (2.5)$$

where $\eta \equiv \frac{v'(x,k)}{-ikv(x,k)}$, so that $r(0, k) = R(k)$ and r has the physical meaning of a reflection coefficient [in the sense of (2.4)] anywhere that $\alpha = 0$. The nonlinear Plancherel equality relating the "energies" of $R(k)$ and $\alpha(x)$ [41], [93], [94] is given by

$$-\int_{-\infty}^{\infty} \log(1 - |R(k)|^2)\,dk = \frac{\pi}{4}\int_{-\infty}^{0} |\alpha(x)|^2\,dx. \qquad (2.6)$$

Direct computation using (2.3) and (2.5) leads to a Riccati equation for the depth-dependent reflection coefficient

$$r'(x, k) = 2ikr(x, k) + \frac{\alpha}{2}[1 - r^2(x, k)] \qquad (2.7)$$

with the boundary condition $\lim_{x \to -\infty} r(x, k) = 0$. Using an integrating factor to formally solve (2.7) yields an integral equation for r

$$r(x_1, k) = r(x_0, k)e^{2ikx_1} - \int_{x_1}^{x_0} e^{2ik(x_1 - y)}\frac{\alpha(y)}{2}[1 - r^2(y, k)]\,dy. \qquad (2.8)$$

We solve the inverse problem via the following observation. If we do not require that causality be satisfied, any choice of $r(x_0, k)$ and $\alpha(x)$ will produce an $r(x_1, k)$. If we insist that causality be satisfied, the previous statement still holds provided $x_1 > x_0$, i.e., when x_1 lies above x_0. However, when x_1 is beneath x_0, i.e., $x_1 < x_0$, there is only one possible choice of $\alpha(x)$ that can combine with a causal $r(x_0, k)$ to produce a causal $r(x_1, k)$. That is, when noncausal results are

excluded, one input (a causal $r(x_0, k)$) can only produce a unique pair of outputs $(\alpha(x), r(x_1, k))$ for $x_1 < x_0$ [94].

While previous layer-stripping methods deduced $\alpha(x)$ via an additional *trace formula* (which always relied on data in the high-frequency limit), we deduce $\alpha(x)$ by simply requiring that $r(x, k)$ correspond to a causal impulse response (as any true physical solution must). To accomplish this, we first define a pair of projection operators that, when applied to a frequency-domain function, project out its causal and acausal parts.

Define Fourier transformation of a function of z to k-space by

$$\hat{f}(k) = \mathcal{F}[f(z)] = \int_{-\infty}^{\infty} e^{-2ikz} f(z) \, dz \qquad (2.9)$$

and the corresponding inverse Fourier transformation by

$$\check{f}(z) = \mathcal{F}^{-1}[\hat{f}(k)] = \frac{1}{\pi} \int_{-\infty}^{\infty} e^{2ikz} \hat{f}(k) \, dk. \qquad (2.10)$$

Define $H_{(a<z<b)}$ to be the characteristic function of the interval (a, b), i.e., that function that is one between a and b and zero elsewhere. From these components, construct the operator

$$P_{(a,b)} \rho(k) = \mathcal{F}[H_{(a<z<b)} \mathcal{F}^{-1}(\rho(k))] \qquad (2.11)$$

where $\rho(k)$ is just a test function. The idea here is to take a function of k, compute its (travel) time-domain counterpart [the innermost operation in (2.11)], select out only that part of the travel-time response in the interval (a, b), and then return that edited response to the frequency domain.

Thus, $P_{(-\infty, x)}$ selects that part of a function that could be caused by events (in our case, reflections) below depth x. (Note that by our choice of coordinates, x is a scaled-depth coordinate rather than a physical time—it is negative and decreasing with increasing depth in, or time lag until the corresponding temporal response of, the reflecting medium.) Correspondingly, $P_{(x,\infty)}$ selects that part of the function due to events above x; because the refractive index is constant above $x = 0$, $P_{(x,\infty)} = P_{(x,0)}$ in our problem. Clearly then, any causal $r(x, k)$ must satisfy

$$P_{(-\infty, x)} r(x, k) = r(x, k) \qquad (2.12)$$

and

$$P_{(x,0)} r(x, k) = 0. \qquad (2.13)$$

From (2.8) then, we must have

$$r(x_1, k) = P_{(-\infty, x_1)} \left[r(x_0, k) e^{2ikx_1} \right.$$
$$\left. - \int_{x_1}^{x_0} e^{2ik(x_1 - y)} \frac{\alpha(y)}{2} [1 - r^2(y, k)] \, dy \right] \qquad (2.14)$$

and

$$0 = P_{(x_1, 0)} \left[r(x_0, k) e^{2ikx_1} \right.$$
$$\left. - \int_{x_1}^{x_0} e^{2ik(x_1 - y)} \frac{\alpha(y)}{2} [1 - r^2(y, k)] \, dy \right]. \qquad (2.15)$$

Equations (2.14) and (2.15) form a pair of equations that we can solve iteratively at each depth step to estimate the unique causal pair $\alpha(x), r(x_1, k)$.

Our iterative solution proceeds as follows. We approximate the r^2 terms in the integrands of (2.14) and (2.15) by the product $r(x_0, k) r(x_1, k)$, thus obtaining a set of (approximate) equations for r at the discrete depths x_0 and x_1. We implement the projection operators in terms of Hilbert transforms by using a numerical algorithm given by [105]. Finally, we choose a sufficiently small depth step to allow approximation of $\alpha(x)$ by a constant (which is unknown *a priori*); we estimate the constant initially from $r(x_0, k)$ alone, plug the estimate into the system of equations to produce an estimate of $r(x_1, k)$ and a refined estimate of the constant, and so on until we obtain a pair $\alpha(x), r(x_1, k)$ that satisfy the (discretized) causality-enforcing equations to within a satisfactory tolerance. We then use $r(x_1, k)$ as the new "data" for the next depth step into the medium. We proceed into the medium until the energy of $r(x, k)$ declines to a negligible fraction of its value just above the reflecting medium. A rigorous, detailed proof of the convergence of this algorithm to the true solution is contained in a forthcoming paper [93]. A third paper explaining our numerical methods, results, and the physical insight available from those results is in preparation [109].

Note that all of the results and methods discussed so far are established rigorously only for the case of a real, square-integrable profile of α, i.e., for a reflecting medium that does not absorb (as sea ice and many other natural media certainly do) and in which there are no abrupt jumps in dielectric properties (as there are, for example, at the upper and, probably, lower surfaces of sea ice). However, the propagation regime in many lossy geophysical media, including in particular sea ice, is nonetheless predominantly a propagating regime—losses are not so high that the intuitive picture of phase and energy transport in electromagnetic waves in sea ice breaks down, and although the boundaries of sea ice are sharp on the length scales of the centimeter-wavelength radiation typically used to probe them, for any data of finite bandwidth, we may approximate the boundaries as rapid but continuous variations in refractive index. Thus, there are at least heuristic reasons to believe that application of our methods to bandlimited sea ice data can yield usefully approximate results. A quantitative investigation of these ideas will appear in a forthcoming publication. For now, we simply note that limited computational and experimental experience supports some optimism. We substantiate this claim briefly below.

1) Analog to the Classical Paley–Wiener Theorem: The Paley–Wiener theorem in classical Fourier analysis relates the growth of the Fourier transform in the frequency domain to the size of the region on which its (inverse) Fourier transform is nonzero. Our analog of this theorem for the reflection problem provides the depth range, in the scaled-coordinate x, over which $\alpha(x)$ is nonzero (i.e., the range of x over which the refractive index varies), as a Fourier transform of a simple nonlinear function of the reflection data [93]. (This result arose more or less as a byproduct of our investigation leading to the preceding results.) Specifically, the width of the region on the

x-axis over which the function

$$W(x) = \mathcal{F}^{-1}\left[\frac{1}{1 - |R(k)|^2}\right] \qquad (2.16)$$

takes nonzero values is equal to the thickness of the depth range, in x, over which the refractive index varies.

Thus, a relatively simple operation, performed directly on data, suffices to determine the scaled thickness of a reflecting layer—a remarkable simplification if we do not require a full estimate of the refractivity profile. The price for this simplicity is that the layer-thickness estimate is given only in scaled depth; conversion to actual physical depth still requires information on the refractive index within the layer.

There are many physical situations, though, in which *a priori* knowledge of the range of possible refractive index profiles suffices to produce an acceptably accurate estimate of physical layer thickness. Suppose that the profile of relative permittivity, i.e., the square of the refractive index, is known on physical grounds not to vary over a range larger than, say, C. Then the average relative permittivity within the layer is between one and C, and the accuracy of conversion from scaled to physical layer thickness depends only the square root of this average. Thus, our analog to the classical Paley–Wiener theorem appears to constitute a useful practical result in its own right.

2) Analysis of Experimental Data: The series of CR-RELEX experiments conducted during the ARI has produced at least two sets of wideband, vertical incidence reflectivity measurements of simulated gray (sea) ice, in addition to indoor laboratory measurements of a layered dielectric system with lower losses and smaller dielectric jumps than those typical of sea ice [42]. Both sets of measurements of simulated sea ice are of high quality, but those by Gogineni and Jezek [42] involve ice of only one, rather large thickness and evidently do not contain frequencies low enough to probe the entire ice thickness, while independent measurements by Onstott [42] for a range of thicknesses lack reflection phase information. We therefore present here a sample application of our methods to the indoor laboratory data from a simplified system that have been gathered by Borup and Johnson (see Section II-B).

Briefly, the laboratory system consisted of a pair of horn antennas suspended over an artificial-layered system. The antennas were arranged to measure vertically polarized reflection at a reflection angle near 10∘. The layered system consisted of two planar layers over a basement. The layers were composed of common gypsum wallboard and styrofoam, measuring 2.54 and 5.59 cm, respectively. The deep (presumably, effectively infinite) basement consisted of sand. Independent, contact-method measurements of the permittivities of the system constituents were not reported to us. Measurements of the complex reflection coefficient of the system at frequencies from roughly 1 to 18 GHz were obtained from stepped-frequency observations. The geometry of the system is represented in Fig. 1. We used these observations directly in a numerical implementation of our inverse method (neglecting for now the slight variation from vertical incidence in the experimental data), with the results shown in Figs. 2–4.
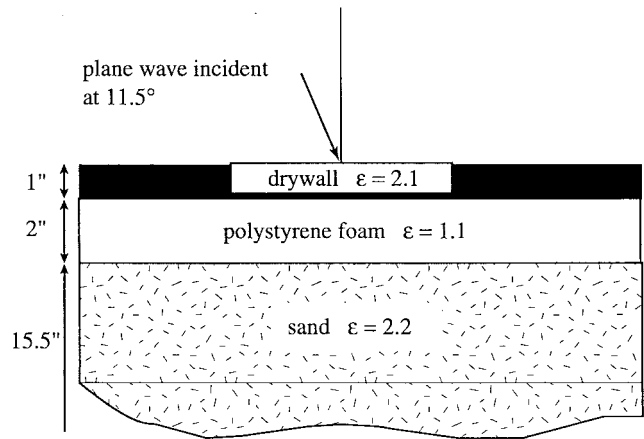

Fig. 1. Geometry of the drywall-polystyrene foam-sand dielectric profile that was scanned from 1 to 18 GHz at an incident angle of 11.5° in the laboratory by Borup and Johnson.

Fig. 2 shows our retrieval of α (solid line) as a function of travel-time (in nanoseconds). Peaks at the boundaries of the wallboard and sand interfaces are the dominant features. For comparison, we also show (dashed line) a retrieval of α produced in exactly the same way as the first, but based on data intentionally made noisier. Specifically, we corrupted Borup and Johnson's data by multiplying each of the real and imaginary parts by one plus a normally distributed random variable having a standard deviation, for given data value, of 70% of that value. Our retrieval of α is clearly stable and robust in the presence of such noise.

Fig. 3 shows our estimate of the profile of refractive index versus physical depth (in centimeters, based on the data as received from Borup and Johnson). Because the observed magnitudes of reflections at the upper edge of the frequency range do approach zero and we have not "tapered" the input data, a modest amount of "ringing" is also apparent in our result. The finite bandwidth of the data causes the transitions between layers in our result to be smoothed. We estimate a permittivity and thickness of the gypsum layer at approximately 2.3 and 2.7 cm, respectively, with the latter figure in particular dependent on a particular interpretation of where our smoothly varying results indicate layer boundaries to lie. Although styrofoam is typically assumed to have a permittivity of very nearly one at microwave frequencies, our inversion suggests a figure closer to 1.1, with a thickness of approximately 4.5 cm, the precise figure again depending on the interpretation of our result. We estimate permittivity of the sand near the styrofoam/sand interface to be two. For comparison, we also plot in Fig. 3 (solid line) the first set of layer permittivity estimates we received from the experimenters—2.3 for the wallboard, one for the styrofoam, and two for the sand. Those estimates resulted from an early application of an alternative reflection inversion method that they had developed. The experimenters later revised their estimates to 2.1 for the wallboard and 2.2 for the sand. A precise test of inversion methods awaits independent information on the true permittivities (and any dispersion) in the layered system.

Finally, Fig. 4 shows an application of our nonlinear analog to the Paley–Wiener theorem to the uncorrupted data (solid
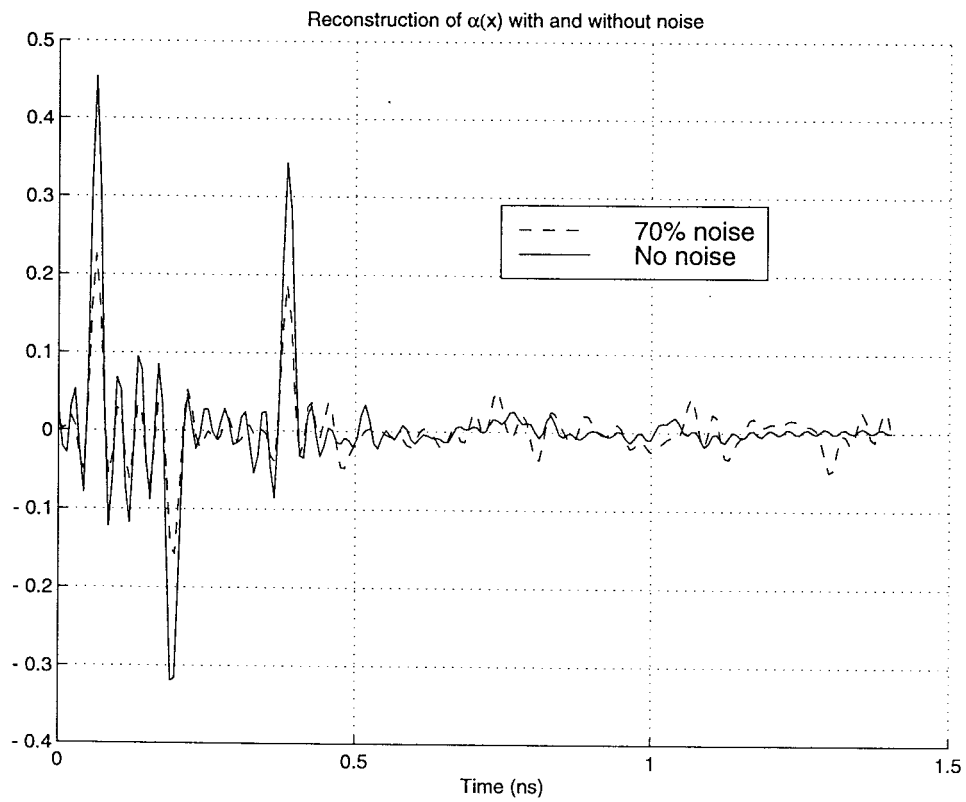
Fig. 2. Causally stabilized layer-stripping reconstruction of the profile of α as a function of travel time in nanoseconds, based on wideband, near-vertical incidence reflectivity data for the layered system of Borup and Johnson (solid line) and on the same data intentionally corrupted with multiplicative noise (dashed line, 70% standard deviation).
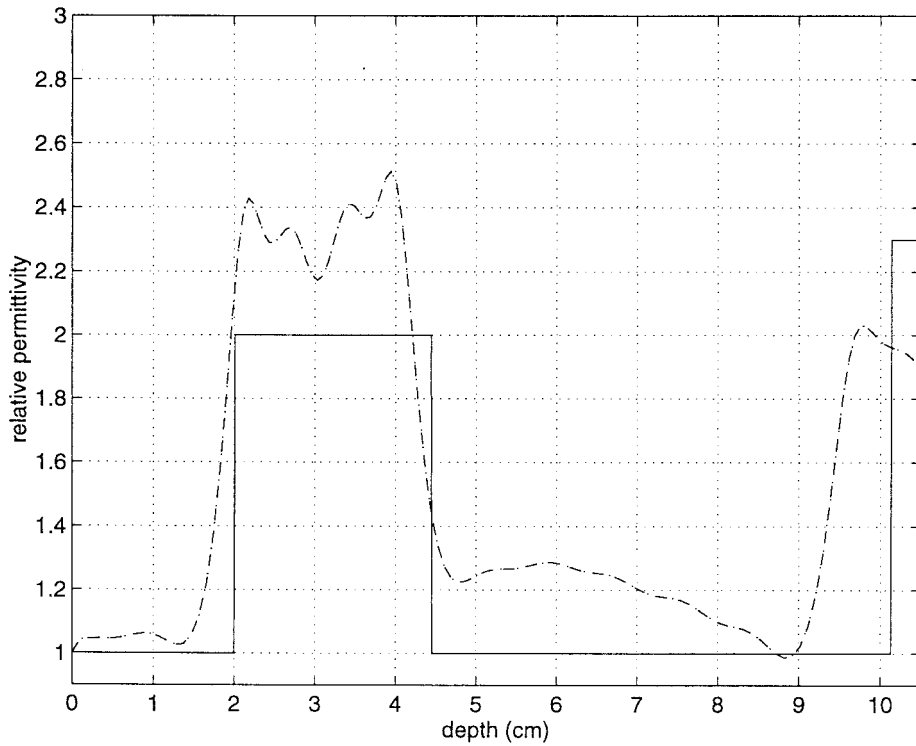

Fig. 3. Causally stabilized layer-stripping reconstruction (dotted) of the depth profile of the (real) relative permittivity $\epsilon(z)$ computed from the data of Borup and Johnson for a layered system.
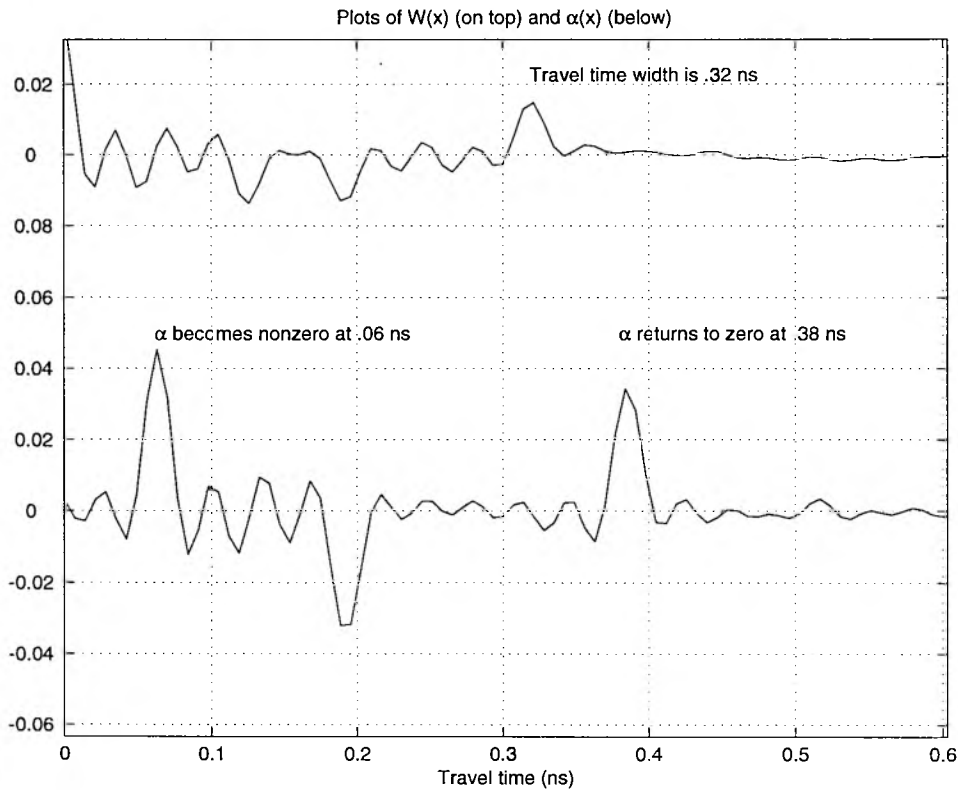
Fig. 4. Application of the nonlinear Paley–Wiener theorem to the reflection data of Borup and Johnson, showing $W(x)$ and $\alpha(x)$ as a function of travel time in nanoseconds.

line). The function $W(x)$ defined above falls essentially to zero at a travel-time thickness of 0.32 ns, which agrees with a travel time thickness indicated in Fig. 2 of approximately 0.32 ns.

B. Inversion by Multilayer Parameter Optimization in One Dimension

In this section, a method for the inversion of 1-D dielectric profiles from electromagnetic scattering data, developed by Borup and Johnson, is presented. The method is based on the minimization of an L^2 least-squares error functional by nonlinear optimization. The forward scattering model employed is derived from the exact scattering solution for an N layer slab [71]. The accuracy of the method is then demonstrated by successfully applying it to laboratory scattering data taken by Borup and Johnson.

We consider the 1-D Helmholtz (2.2) with real permittivity $\epsilon(z) = n^2(z)$ and the exact solution for a layered medium that will be used in the inversion. Assume that the medium has layers $j = 0, 1, \ldots, N + 1$, with indexes of refraction n_j, and that layer 0 is a homogeneous half space $z > 0$ of air with $n_0 = 1$ and layer $N + 1$ is a homogeneous half space extending to $z = -\infty$ with index of refraction n_{N+1}. Each of the N finite layers is assumed to have uniform thickness h. As described above, we consider a TE wave with an angle of incidence θ, which we assume for now is $\theta = 0$. The wave field u represents E_2 in $\mathbf{E} = (0, E_2, 0)$. In each layer, the solution $u_j(z)$ is the sum of a forward and a backward

propagating plane wave

$$u_j(z) = a_j e^{-ikn_j z} + b_j e^{ikn_j z}, \quad -jh \leq z \leq -(j-1)h \tag{2.17}$$

where k is the free-space wavenumber and $j = 1, \ldots, N$. At each interface $z = -jh$, continuity of E_2 and the magnetic field H_1 in $\mathbf{H} = (H_1, 0, 0)$ yields a recursion relation for $\mathbf{a}_j = (a_j, b_j)$ of the form

$$\mathbf{a}_j = \mathbf{K}_j \mathbf{a}_{j+1} \tag{2.18}$$

where the coefficients of the matrix $\mathbf{K}_j$ involve j, h, n_j, and n_{j+1}. Using $a_0 = 1$ and $b_{N+1} = 0$ allows us to solve for the reflection coefficient $R(k) = b_0$. This recursive scheme requires only $O(N)$ arithmetic operations, as opposed to $O(N^3)$, required to solve via the moment method the 1-D scattering integral equation

$$u(z) = u^i(z) - \frac{k}{2i} \int_0^{Nh} e^{-ik|z-z'|} \gamma(z') u(z') \, dz' \tag{2.19}$$

where

$$\gamma(z) = \epsilon(z) - 1 = n^2(z) - 1 \tag{2.20}$$

and u_i is the incident field. We note that for an incidence angle different than zero, we replace k with $k \cos \theta$ and n_j^2 with $n_j^2 - \sin^2 \theta$.

Now, given a vector $\gamma = (\gamma_1, \ldots, \gamma_N)$ of dielectric parameters and an incidence angle θ, the above solution can be used to exactly calculate the complex reflection coefficient $R_\theta^{\text{calc}}(k, \gamma)$

for the given N layer slab. The idea of the inversion scheme is to find a γ that minimizes the mean square (L^2) error between the measured scattering data and that calculated from the forward model above. The scattering data is defined as the rescaled complex reflection coefficient

$$\Psi_\theta(k) = \frac{2i \cos \theta}{k} R_\theta(k). \tag{2.21}$$

Then the reconstruction of the dielectric profile consists of applying nonlinear minimization to the functional

$$F(\gamma) = \sum_{k,\theta} \left| \Psi_\theta^{\text{calc}}(k, \gamma) - \Psi_\theta^{\text{meas}}(k) \right|^2 \tag{2.22}$$

where γ is the vector of unknown dielectric parameters. The minimization of $F(\gamma)$ is carried out using the Ribere–Polack algorithm [81]. This algorithm is a variant of the conjugate gradient algorithm for the minimization of a nonquadratic functional. It requires a subroutine for computing the gradient of the functional, as opposed to Newton's method, which requires the Hessian.

The number of computations needed to compute the reflection coefficient for one incident angle at one frequency is $O(N)$. For K wavenumbers (or frequencies) and Θ angles of incidence, the computation is $O(\Theta K N)$. To minimize the functional (2.22) via the Ribere–Polack algorithm, we need to compute its gradient

$$\nabla F(\gamma) = J(\gamma) \mathbf{r}(\gamma) \tag{2.23}$$

where J is the Jacobian of the model equations and $\mathbf{r}$ is a unit vector in the direction in γ-space of greatest increase in $F(\gamma)$. It turns out that a recursive algorithm for this calculation can be derived from the 1-D layered slab solution for a given $\mathbf{r}$ and γ. Thus, explicit computation and storage of the Jacobian is not needed, and the resulting gradient calculation algorithm is also $O(\Theta K N)$. Thus, a single iteration of the Ribere–Polack minimization algorithm requires only $O(\Theta K N)$ computations. The memory storage requirement is $O(\Theta K)$.

We note that the rescaling of the scattering data in (2.21) is suggested by the Born approximation, which gives

$$\begin{aligned} R(k, \theta) &= \frac{k}{2i \cos \theta} \int_0^\infty \gamma(z) e^{-2ik \cos \theta z} \, dz \\ &= \frac{k}{2i \cos \theta} \hat{\gamma}(2k \cos \theta) \end{aligned} \tag{2.24}$$

where $\hat{\gamma}$ denotes the Fourier transform of γ. Thus, for real scattering potentials ($\gamma(z) = \epsilon(z) - 1$) and for one angle of incidence at $\theta = 0°$, the rescaling in (2.21) gives a linear, unitary (Fourier transform) equation

$$\Psi_{\theta=0}(k, \gamma(z)) = \hat{\gamma}(2k). \tag{2.25}$$

Thus, for real scattering potentials satisfying the Born approximation, the Ribere–Polack algorithm will converge in one step [because (2.25) is unitary] if the frequency content of the data (bandwidth) is sufficient. Note that (2.25) cannot be inverted for a frequency-independent, complex $\gamma(z)$ because the data determine only the positive spatial frequencies in the Fourier domain. For the real dielectric constant case, (2.25) can be inverted since $\hat{\gamma}(-k) = \overline{\hat{\gamma}(k)}$ for real γ. In the Ribere–Polack

algorithm, this realness condition can be enforced by simply zeroing the imaginary part of the gradient (2.23) each time it is computed.

Analysis of the Born approximation and numerical experiments in the real dielectric constant case has shown that the bandwidth requirement for a single, normally incident plane wave is

$$\frac{\lambda_{\max}}{2} \geq Nh, \quad \lambda_{\min} \leq 4h \tag{2.26}$$

i.e., the maximum wavelength in the medium should be one-half the thickness of the problem and the spatial sample increment of the reconstruction should be set at one-quarter the minimum wavelength. In terms of frequency, and for multiple view angles, we require

$$f_{\min} \leq \frac{c}{2T \cos \theta_{\max}}, \quad \frac{c}{2h \cos \theta_{\min}} \leq f_{\max} \tag{2.27}$$

where $T = Nh$ is the depth (thickness) of the layered slab, c_{slab} is a phase speed in the slab, and $\theta_{\min}$, $\theta_{\max}$ are the minimum and maximum incident angles in the data set.

Results: Fig. 1 shows the geometry of a 1-D real dielectric profile, which was constructed in the laboratory. The profile consists of a 1″ slab of construction drywall and a 2″ slab of polystyrene foam placed on top of a 15.5″ deep layer of sand. The reflection coefficient of the profile was measured at an incident angle of 11.5° using two 1–18-GHz, ridged horn antennas and a network analyzer. Calibration for the antenna transfer functions was achieved by first collecting the reflection data for a 1/8″ sheet of aluminum placed on top of the drywall. The data without the metal plate was then divided by the metal plate data and multiplied by −1 (the plane wave reflection coefficient of a perfectly conducting plane is −1). This procedure calibrates the frequency-domain data to match plane wave theory.

The exact solution for a three-layer model was then computed, and the three dielectric parameters ϵ(drywall), ϵ(foam), ϵ(sand), and the two thicknesses, T(drywall) and T(foam), were optimized for by trial and error, comparing the resulting time-domain signal visually with that for the collected data. The best visual fit to the data was found to be ϵ(drywall) = 2.1, ϵ(foam) = 1.1, ϵ(sand) = 2.2, T(drywall) = 1″, and T(foam) = 2.1″. An excellent match between the theory and the data in the time domain was achieved, indicating a successful calibration of the 1-D scattering experiment.

The data were then inverted using a 40-element, $h = 3$ mm, numerical model of the dielectric profile. The Ribere–Polack algorithm was able to match the data to within 14% rms error. The algorithm would reduce the error no further and the normalized gradient magnitude was <0.001, indicating that the remaining 14% mismatch consists of data components outside of the range of the forward model. Fig. 5 compares the inverted solution with the true solution (based on the visually optimized parameters discussed above).

Thus, a 1-D dielectric profile inversion method based on the exact scattering solution for an N layer slab has been developed and verified for laboratory data. The method requires a wide bandwidth of data—the minimum frequency should be such that the unknown thickness to be inverted is less
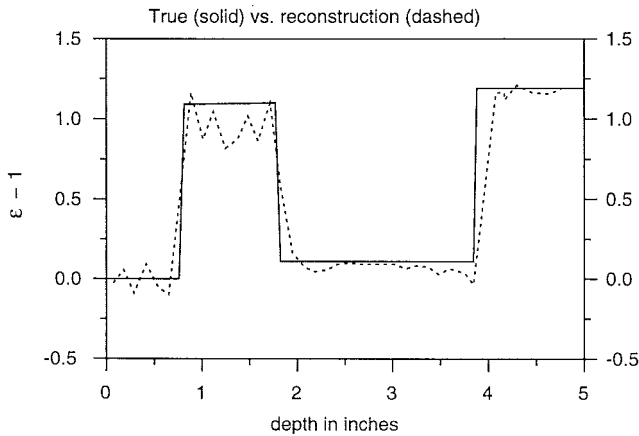
True (solid) vs. reconstruction (dashed)

Fig. 5. Multilayer parameter optimization reconstruction (dotted) of the depth profile of the (real) relative permittivity $\epsilon(z) - 1$ computed from the data of Borup and Johnson for a layered system.

than or equal to one-half the maximum wavelength, and the resolution of the inversion is given by one half the minimum wavelength (2.26). Present efforts are aimed at the inversion of lossy media. In particular, data from partially water-saturated foam rubber has been collected. Thus far, the authors have been unable to accurately match this data to theory. Attempts to invert simulated data from lossy media have been made, and it has been found that this problem is considerably less well-posed than the case of a lossless dielectric. Efforts to constrain the dispersion of the dielectric to be causal, i.e., by enforcing the satisfaction of the Kramers–Kronig relations [74], are being investigated as a possible solution to this ill-posedness.

C. Inversion by Layer Stripping in Higher Dimensions

The problem of reconstructing the complex permittivity $\epsilon(\mathbf{x})$ of a complicated medium, such as the sea ice system, from electromagnetic scattering data, has a mathematical structure similar to the impedance imaging problem of reconstructing the local conductivity $\sigma(\mathbf{x})$ of an object from boundary measurements of the potential induced by an applied current density. Due to the importance of impedance imaging to such areas as nondestructive materials testing, geophysical prospecting, process control, and medical imaging, there has been substantial work on this problem both from the theoretical as well as computational and practical points of view (see [88] for numerous references). For example, the lungs can be monitored through impedance images of the conductivity profile of the chest obtained from data provided by electrodes on the skin [50]. In [88], a direct method was developed to find the conductivity inside a body. The algorithm proceeds via two steps. First, the conductivity near the surface of the body is found, and then the boundary data on an interior surface are synthesized using a Riccati equation. The process is repeated, and an estimate of the interior conductivity is found, layer by layer. In [16], such an approach has been developed for the electromagnetic inverse scattering problem for the sea ice system, treated as a perturbed, dissipative half space. The forward scattering theory necessary for this development was presented in [16] and [41].

To describe the inverse scattering algorithm for the sea ice system, it is useful to briefly consider the impedance imaging problem [88] for a body with local conductivity $\sigma(\mathbf{x})$ occupying a region $\Omega \subset \mathbf{R}^d$, $d = 2$ or 3, with a smooth boundary $\partial\Omega$. The electric potential $\phi(\mathbf{x})$ satisfies $\nabla \cdot \sigma\nabla\phi = 0$ in Ω and $\sigma\partial_\nu\phi = j$ on $\partial\Omega$, where ∂_ν denotes the exterior normal derivative at the boundary and j is the current density applied to the boundary. We assume that we can apply any current density j to the boundary and measure the corresponding voltage ϕ at every point on the boundary. In other words, we know the *resistive* map

$$\mathcal{R} : j \mapsto \phi|_{\partial\Omega} \tag{2.28}$$

which is a linear operator on sufficiently smooth functions on the boundary, in particular, $\mathcal{R} : H^s(\partial\Omega) \mapsto H^{s+1}(\partial\Omega)$, where $H^s(\partial\Omega)$ is the L^2 based Sobolev space on $\partial\Omega$ with smoothness index s. For the impedance imaging problem, working with $\mathcal{R}$ is more stable than working with its inverse Λ, called the Dirichlet-to-Neumann map

$$\Lambda : \phi|_{\partial\Omega} \mapsto j. \tag{2.29}$$

(The Dirichlet data of a function on Ω is its set of boundary values, and the Neumann data it the set of boundary values of its normal derivative.) The inverse boundary value problem is to reconstruct $\sigma(\mathbf{x})$ from partial knowledge of the resistive operator $\mathcal{R}$ on $\partial\Omega$. Such maps have been used a great deal recently in the study of inverse problems, e.g., [16], [88], and [92]. The layer-stripping algorithm for impedance imaging is based on first reconstructing $\sigma(\mathbf{x})$ on the boundary from $\mathcal{R}$ and then synthesizing $\mathcal{R}$ on a subsurface infinitesimally close to the boundary. This continuation can be accomplished because $\mathcal{R}$ satisfies a (nonlinear) differential equation, of Riccati type. The method accounts fully for the nonlinear nature of the inverse problem.

We now turn our attention back to inverse scattering theory for (2.1) with dissipation

$$\nabla^2 u + (k^2 n^2 + ikm)u = 0 \tag{2.30}$$

where $u = E_2$ for a TE wave. We assume $n = 1, m = 0$ for $x_3 \geq 0$, while in the lower half-space $x_3 < 0$. n differs from a positive constant n_- only in a region of compact support and m differs from a positive constant m_- only in this region as well [16]. To apply the layer-stripping approach developed for the impedance imaging problem, we must first obtain the scattering operator $\mathcal{S}$ mapping incident to scattered fields, which plays the role of $\mathcal{R}$ or Λ above. Then the inverse scattering problem is to reconstruct n and m from partial knowledge of $\mathcal{S}$.

To define the **scattering operator** $\mathcal{S}$, we consider the wave field u in the upper half space. Then $\mathcal{S}$ is the map from the down-going part of the wave field to the up-going part. We construct an explicit representation $\hat{\mathcal{S}}$ of this map in the Fourier transform domain. In particular, we use the fact that the medium parameters are known and constant in the upper half space. For x_3 positive, we can therefore Fourier transform (2.30) in the x_1 and x_2 coordinates. The result is an ordinary

differential equation whose general solution for $x_3 > 0$ is

$$\hat{u}(\kappa, x_3) = A(\kappa)e^{-i\lambda_+ x_3} + B(\kappa)e^{i\lambda_+ x_3} \qquad (2.31)$$

where $\lambda_+ = \sqrt{k^2 - |\kappa|^2}$ and the hat denotes the 2-D Fourier transform

$$\hat{u}(\kappa, x_3) = \int u(\mathbf{x}', x_3)e^{-i\kappa \cdot \mathbf{x}'} d\mathbf{x}' \qquad (2.32)$$

with $\mathbf{x}'$ denoting (x_1, x_2). When λ_+ is zero, the general solution corresponding to (2.31) is simply linear function of x_3. When $|\kappa| < k$, the A term in (2.31) is a down-going wave, whereas the B term is up-going. The coefficient A thus determines an incident wave. This incident wave, together with continuity of u and its normal derivative at the interface $x_3 = 0$ and a radiation condition in the lower half-space, uniquely defines the scattered wave, which determines B. Consequently, we can define $\hat{S}$ as the map from $A(\kappa)$ to $B(\kappa)$.

The inverse algorithm for the impedance imaging problem is based on a Ricatti equation for the resistive map associated with the inverse boundary value problem. Application of this approach to the inverse scattering problem relies on an equivalent formulation of the scattering problem as a **boundary value problem**, defined by (2.30) for $x_3 < 0$ with the boundary condition $u|_{x_3=0} = f(x_1, x_2)$, together with an out-going radiation condition in the lower half space. If f is in the Sobolev space $H^{1/2}$ and $m > 0$, the Lax–Milgram theorem can be used to show that this boundary value problem has a unique H^1 solution in the lower half space. Thus, the normal derivative $\partial_\nu u$ on the surface $x_3 = 0$ is uniquely determined. The mapping

$$\Lambda : u\big|_{x_3=0} \mapsto \partial_\nu u\big|_{x_3=0} \qquad (2.33)$$

from $H^{1/2}$ to $H^{-1/2}$ is the Dirichlet-to-Neumann map for this problem. The inverse boundary value problem is to determine n^2 and m from knowledge of Λ. This boundary value formulation with Λ is related to the scattering formulation with $\mathcal{S}$ as follows. Define $\hat{\Lambda}$ via $\widehat{\Lambda f} = \hat{\Lambda}\hat{f}$. Then it can be shown that

$$\hat{\Lambda}(\hat{S} + I) = i\lambda_+(\hat{S} - I) \qquad (2.34)$$

which holds as an operator equation in an appropriate function space [16]. This relation can be used to find $\hat{S}$ in terms of $\hat{\Lambda}$, or vice versa.

1) Layer-Stripping Algorithm: Now, the idea of the method to solve the inverse scattering problem for (2.30) is to use the measured data to find the medium parameters on the boundary $x_3 = 0$, then to use that information to synthesize data on a nearby inner subsurface. The process is then repeated, and the medium parameters are found layer by layer. To synthesize the subsurface data, we obtain a differential equation for Λ in the depth variable. This requires that we extend the definition of the Dirichlet-to-Neumann map to any $z < 0$

$$\Lambda(z)u\big|_{x_3=z} \equiv \frac{\partial u}{\partial x_3}\bigg|_{x_3=z}. \qquad (2.35)$$

This map then satisfies the following Riccati equation:

$$\frac{d\Lambda}{dz} = -\Lambda^2 - (\partial_{x_1}^2 + \partial_{x_2}^2) - k^2\epsilon \qquad (2.36)$$

with $\epsilon = n^2 + im/k$. This equation is obtained by differentiating (2.35) with respect to z, using (2.30) to eliminate $\partial^2 u/\partial z^2$ and (2.35) to eliminate $\partial u/\partial z$. A similar equation can be obtained for $\hat{S}$.

The layer-stripping algorithm proceeds by first finding the medium parameters on the surface and then using (2.36) to continue the recovery process into the interior. To find the medium parameters on the surface, we use the following time-domain approach. This will be discussed again, in more detail, below. The time-domain version of (2.30), in the variable $\tau = ct$, is

$$(\nabla^2 - n^2\partial_\tau^2 - m\partial_\tau)\mathcal{U} = 0. \qquad (2.37)$$

The plan is to obtain a progressing wave expansion [24] for (2.37). We are interested in the small-time behavior of $\mathcal{U}$ in the neighborhood of an interface at $x_3 = 0$. For $x_3 > 0$, where $n = 1$, we expect that $\mathcal{U}$ is composed of an incident plane wave $\mathcal{U}^i = \delta(s^i(\mathbf{x}) - \tau)$ plus a reflected wave, which we expand in the form

$$\mathcal{U}^r(s^r(\mathbf{x}) - \tau) = A_0^r(\mathbf{x})\delta(s^r(\mathbf{x}) - \tau) \\ + A_1^r(\mathbf{x})H(s^r(\mathbf{x}) - \tau) + \cdots. \qquad (2.38)$$

Here s^i and s^r are the incident and reflected phases, δ denotes the Dirac delta function, and H denotes the Heaviside function that is one for positive arguments and zero for negative arguments. We take $\mathcal{U}^i$ to be a plane wave propagating in direction $\mathbf{e} = (e_1, e_2, e_3)$, which implies that $s^i = \mathbf{e} \cdot \mathbf{x}$. Because we take this wave to be propagating in the downward direction, e_3 is negative. Just below the interface, for a short time, we expect $\mathcal{U}$ to take the form of a transmitted wave, which we also expand as

$$\mathcal{U}^t(s^t(\mathbf{x}) - \tau) = A_0^t(\mathbf{x})\delta(s^t(\mathbf{x}) - \tau) \\ + A_1^t(\mathbf{x})H(s^t(\mathbf{x}) - \tau) + \cdots. \qquad (2.39)$$

Here again s^t denotes the phase of the transmitted wave.

On the interface $x_3 = 0$, $\mathcal{U}$ and its first x_3 derivative are continuous. Using these conditions at the interface and forcing $\mathcal{U}$ to satisfy (2.37) results in expressions for the coefficients in (2.38) and (2.39) [16]. The expressions for A_0^r and A_0^t at $x_3 = 0$ involve $\mathbf{e}$ and n, while the expression for A_1^r involves $\mathbf{e}, m, n$ and the derivatives of A_0^r and A_0^t.

To obtain the medium parameters n^2 and m at a point $\mathbf{x}_0$ on the surface from scattering data, we send in an incident wave that is planar in a neighborhood of $\mathbf{x}_0$. We then measure the scattered field at all points on a plane $x_3 = $ constant. From this information, the short-time scattered field can be inferred in a neighborhood of x^0 and thus the value of A_0^r at $\mathbf{x}_0$, which tells us the value of n^2 at $\mathbf{x}_0$. In this manner, we obtain n^2 for every point on the surface; this allows us to compute, at every point, not only A_0^t, but also the derivatives in the expression for A_1^r, which can then be used to obtain m as well.

Having found the medium parameters on the surface, the algorithm can proceed. Let us consider the layer-stripping algorithm in the case when a complete set of incident fields are used and measurements of the corresponding scattered fields are made on a plane. We assume measurements are made at N frequencies. For experiments with stepped-frequency radar,

for example, N can range from 51 to 801. The algorithm proceeds as follows.

1) From the measurements at wavenumbers $k_0, k_1, \ldots, k_N$, construct an approximation to each scattering operator $\mathcal{S}(k_n)$, $n = 0, 1, \ldots, N$ (the integer index n here should not be confused with the index of refraction n). In practice, we would represent $\mathcal{S}(k_n)$ by its matrix with respect to some basis. Such a basis could perhaps be constructed from antenna beam patterns for a large number of incident angles. The operator $\hat{\mathcal{S}}$ of (2.34), for example, is the representation of $\mathcal{S}$ in a Fourier basis.

2) For each of at least two incident directions $\mathbf{e}_j$, $j = 1, 2, \ldots, J$, choose an incident field that looks like $\exp(ik_n \mathbf{e}_j \cdot \mathbf{x})$ in the neighborhood of some point $\mathbf{x}_0$ on the surface. Apply $\mathcal{S}(k_n)$ to these incident fields to obtain the scattered field $u_{\mathrm{sc}}(k_n, \mathbf{x})$.

3) Fourier transform into the time domain to obtain $U^r(\tau, \mathbf{x})$. In practice, we can do this by first synthesizing an approximate delta function in the form

$$\delta(\tau) \approx \sum_{n=1}^{N} w_n e^{ik_n \tau} \tag{2.40}$$

where the w_n are, for example, Hamming weights [76]. Then the field

$$U^r(\tau, \mathbf{x}) \approx \sum_{n=1}^{N} u_{\mathrm{sc}}(k_n, \mathbf{x}) w_n e^{ik_n \tau} \tag{2.41}$$

is locally the response to the incident approximate delta function (2.40), where u_{sc} is the scattered field.

4) Extract the coefficients $A_0^r(\mathbf{x}_0, \mathbf{e}_j)$ and $A_1^r(\mathbf{x}_0, \mathbf{e}_j)$. This can be done, for example, by the least-squares minimization

$$\min_{A_0^r, A_1^r} \int_0^T \left| U^r(\tau, \mathbf{x}_0) - A_0^r(\mathbf{x}_0, \mathbf{e}_j) \delta(s^r(\mathbf{x}_0) - \tau) \right.$$
$$\left. - A_1^r(\mathbf{x}_0, \mathbf{e}_j) H(s^r(\mathbf{x}_0) - \tau) \right|^2 d\tau \tag{2.42}$$

where for U^r one uses (2.41), for s^r one uses $s^r = e_1 x_1 + e_2 x_2 - e_3 x_3$, for δ one uses (2.40), and for the Heaviside function H one uses

$$H(\tau) \approx \sum_{n=1}^{N} \frac{w_n}{ik_n} e^{ik_n \tau}. \tag{2.43}$$

5) From $A_0^r(\mathbf{x}_0, \mathbf{e}_j)$ and $A_1^r(\mathbf{x}_0, \mathbf{e}_j)$ for $j = 1, 2, \ldots, J$, determine $n^2(\mathbf{x}_0)$, $m(\mathbf{x}_0)$, and $\partial_{x_3} n^2(\mathbf{x}_0)$. If $J > 2$ so that the system is overdetermined, we can use least squares to find the best fit.

6) Repeat steps 2)–5) for a large number of points $\mathbf{x}_0$ on the surface.

7) For each k_n, synthesize the subsurface data either from a Riccati equation for $S(k_n)$ or use (2.34) to convert $S(k_n)$ to $\Lambda(k_n)$, use the Riccati (2.36), and convert back to $S(k_n)$ with (2.34). Again, in practice, the operators $S(k_n)$ and $\Lambda(k_n)$ would be represented as matrices with respect to some basis, and (2.34) and (2.36) would be approximated as matrix equations.

8) Repeat, starting with step 2).

Although the above algorithm may seem ready to implement, it cannot be used in its present form because it is *unstable*. This is partly because of the multiplication by $|\kappa|^2$ in the Riccati equation for $\hat{\mathcal{S}}$ [16] or, equivalently, because of the x_1 and x_2 derivatives appearing on the right side of (2.36). This is similar to the situation in [111]; this type of instability can be overcome to some extent by smoothing in the x_1 and x_2 directions, as discussed in [15]. Even when the problem is independent of x_1 and x_2, however, we expect the methods to be unstable, due to the fact that only a little of the energy put into the system on the top can propagate to great depths. Thus, we expect the boundary data and scattering data to contain little information about the deeper regions.

2) Recovery of Surface Parameters: We return to the algorithm for reconstructing the medium parameters n^2 and m on the surface, and we consider the important special case in which the medium is homogeneous near the surface. Refer to [17] for the details. In the case of near surface homogeneity, we have simply

$$A_0 = \frac{1-n}{1+n}, \quad A_1 = \frac{(m + \partial_z n)}{n(1+n)^2}. \tag{2.44}$$

In dealing with data from a stepped-frequency radar, we have measurements from only a finite number of frequencies $k_0, k_1, \ldots, k_N$. For the reflection coefficient we use

$$\Re(\tau) = \sum_n R(k_n) w_n e^{-ik_n \tau}. \tag{2.45}$$

With $k_n = k_0 + n\frac{B}{N}$, where B is the bandwidth (again, the integer index n is not be confused with the index of refraction n), each term of (2.45) contains a factor $e^{-ik_0 \tau}$, and we consider $f(\tau) = e^{ik_0 \tau} \Re(\tau)$. In place of the delta and Heaviside functions in the progressing wave expansion, we use appropriate (factored) versions $p(\tau)$ and $h(\tau)$ of (2.40) and (2.43), respectively. It can be shown [17] that

$$f(\tau) = A_0 p(\tau) + A_1 h(\tau) + r(\tau) \tag{2.46}$$

where r denotes a remainder term that is continuous and zero at the origin. The left side of (2.46) is known from measurements; from it we want to extract A_0 and A_1. To do this, we minimize the least-squares error

$$\int_0^T |f(\tau) - A_0 p(\tau) - A_1 h(\tau) - r(\tau)|^2 d\tau. \tag{2.47}$$

Differentiating with respect to A_0 and A_1 leads to a system of equations for $A = (A_0, A_1)^t$ (the superscript t denotes transpose)

$$MA + Q = F \tag{2.48}$$

where Q is a remainder term assumed small (when T is small). It can be shown that F and the entries of the matrix M are given by

$$F = \left(\mathrm{Re} \sum_{n,m=0}^{N} w_n w_m R_m y_{n-m}, \right.$$
$$\left. \mathrm{Re} \sum_{n,m=0}^{N} w_n \frac{w_m}{ik_n} R_m y_{n-m} \right)^t \tag{2.49}$$

$$M_{11} = \sum_{n,m=0}^{N} w_n w_m y_{n-m}, \quad M_{22} = \sum_{n,m=0}^{N} \frac{w_n w_m}{k_n k_m} y_{n-m}$$

$$(2.50)$$

$$M_{12} = M_{21} = \text{Re} \sum_{n,m=0}^{N} w_n \frac{w_m}{i k_m} y_{n-m} \qquad (2.51)$$

where

$$y_n = \int_0^T e^{\text{in}\tau B/N} d\tau = \begin{cases} T, & \text{if } n = 0 \\ \frac{e^{\text{in}TB/N}}{\text{in}B/N}, & \text{if } n \neq 0. \end{cases} \qquad (2.52)$$

In summary, the method to reconstruct the surface parameters is as follows. Measure the reflection coefficient R_n, $n = 0, \ldots, N$ for the available (equally spaced) frequencies. Use (2.49) and (2.52) to construct F. Solve the equation $MA = F$, where M is given by (2.50) and (2.51), to obtain $A = (A_0, A_1)$. Solve (2.44) for n and m, assuming that $\partial_z n(z) = 0$.

To determine the possible utility of the bandlimited geometrical optics method, it has been tested on synthetic data. To generate the data, we used the well-known formula [55] for the reflection coefficient from a two-layer medium, consisting of a slab of thickness T with medium parameters n and m, overlying a half space with parameters n_- and m_-. This two-layer medium lies underneath a half space of air with parameters $n_+ = 1$ and $m_+ = 0$. After computing the two-layer reflection coefficient, we added random noise, with magnitude α, to the real and imaginary parts. We then used the bandlimited geometrical optics method above to reconstruct n^2 and σ. In each case, we used the same values of n^2 and m to compute the data, namely, $n^2 = 3.37$ and $\sigma = 0.017$. We considered two different frequency bands, namely, 1–4 and 26.5–40 GHz. Because the longer wavelength waves penetrate deeper into the medium, we also considered media of different depths. We chose the T in (2.47) and (2.52) to be $\pi/(2B)$. The results are discussed in detail in [17]. In general, for thick enough samples, agreement was obtained for both n^2 and σ.

We have also made some preliminary tests of this method on experimental data. The data were collected using an HP8510 network analyzer. The data were composed of $N = 801$ measurements of the reflection coefficient, for equally spaced frequencies between 26.5 and 40 GHz. To use these data, we first did some processing to correct for the system response. When we then used the bandlimited geometrical optics method, we obtained a value of $n^2 = 2.42$ for a lucite sample versus $n^2 = 2.48$, as computed by the "bounce" method of [61], [82]. The method did not return a reasonable value for m.

III. INVERSE HOMOGENIZATION AND THE RECOVERY OF MICROSTRUCTURAL PARAMETERS

A. Forward and Inverse Homogenization for Composite Materials

In the previous section, we considered inverse algorithms designed to reconstruct the complex permittivity profiles of inhomogeneous media. Ideally, given scattering data over all frequencies, these algorithms can completely reconstruct the local complex permittivity $\epsilon(\mathbf{x})$, from which the details of the microstructure would become apparent. In the sea ice system, such microstructural details could include the following: brine and air volume fractions, brine and air inclusion size and connectedness properties, sea ice grain size and texture, snow grain size and texture, volume fraction and connectedness of liquid brine in snow or slush, anisotropy and brine microstructure orientation, and crack size and orientation distributions. In practice, however, often we only have available information in a particular frequency band, which may be relatively narrow. In the microwave regime, it is frequently the case that the wavelengths involved are much larger than the scale of some of the features listed above, such as at C-band (with a center frequency of 5.3 GHz). With a free-space wavelength of 5.7 cm, the brine microstructure, with variations on a sub-millimeter scale, cannot be resolved and the wave propagates primarily according to effective electromagnetic parameters. In this case, the reconstructed complex permittivity will be an effective complex permittivity ϵ^*, which itself may vary on larger scales resolvable by the wave, due to variations in the average microstructural properties that determine ϵ^*. For example, a 1-D reconstruction at C-band of the complex permittivity profile $\epsilon^*(z, k)$ of a slab of sea ice, over a range of wavenumbers k, would vary primarily due to the depth (z) variation of the brine volume. If we desire microstructural information about the sea ice, such as the brine volume, it has to be further extracted from the reconstructed profile $\epsilon^*(z, k)$. A general theory of how to obtain microstructural properties from known values of effective electromagnetic characteristics is of clear importance for inversion of sea ice parameters. Furthermore, such techniques would likely have application to other areas where inverse scattering has been useful, such as medical imaging, nondestructive testing of materials, and geophysical exploration. For example, recovery of brine volume information from measurements of ϵ^* is similar to the problem of monitoring fluid volume fraction in the lungs from bulk electrical measurements. Recovery of brine inclusion connectedness is similar to monitoring the porosity of bones or oil bearing rocks as well as to testing the quality of a tenuous conducting matrix in some smart composites of an insulating host with conducting inclusions [38].

Here we develop a rigorous theory of inverse homogenization for composite materials in the quasistatic regime, in which microstructural information about the composite is inverted from measurements of effective electromagnetic properties, such as the complex permittivity ϵ^*. Our approach is based on the Stieltjes integral representation for ϵ^* and its spectral measure μ associated with the composite geometry, presented in [36] and [41] and the resulting forward bounds on ϵ^* incorporating given information on the microstructure. First, we present a theorem, giving the conditions under which μ and the statistical properties of the microstructure can be uniquely reconstructed [18]. Then, we analytically invert the complex elementary and Hashin–Shtrikman bounds R_1 and R_2, considered in [41, Section III], to obtain *inverse bounds* on the brine volume of sea ice (or the relative volume fractions of any two component composite), for given complex permittivity data [19]. We obtain both rigorous bounds on the possible

range of volume fractions given a single value of the observed complex permittivity, valid in the quasistatic regime, and an accurate algorithm for predicting the brine volume associated with a given data set of permittivity values. The algorithm is demonstrated on a representative data set at C-band from [2], with excellent results. We have also inverted the tighter matrix-particle bounds R_1^{mp} and R_2^{mp} for separation information about the brine inclusions, which indicates the connectedness of the brine phase [77].

For completeness, we briefly review the forward homogenization problem [41]. Consider a two-phase random medium in all of $\mathbf{R}^d$, with an isotropic local complex permittivity $\epsilon(\mathbf{x}, \beta)$, taking values ϵ_1 and ϵ_2, the permittivities of brine and ice, respectively, with $\epsilon(\mathbf{x}, \beta)$ a stationary random field in $\mathbf{x} \in \mathbf{R}^d$ and $\beta \in \Omega$, where Ω is the set of all realizations of the random medium. We write $\epsilon(\mathbf{x}, \beta) = \epsilon_1 \chi_1(\mathbf{x}, \beta) + \epsilon_2 \chi_2(\mathbf{x}, \beta)$, where χ_1 is the characteristic function of medium 1 and $\chi_2 = 1 - \chi_1$. Let $\mathbf{E}(\mathbf{x}, \beta)$ and $\mathbf{D}(\mathbf{x}, \beta)$ be the stationary random electric and displacement fields, related by $\mathbf{D} = \epsilon \mathbf{E}$, satisfying $\nabla \cdot \mathbf{D} = 0$ and $\nabla \times \mathbf{E} = \mathbf{0}$, where $\langle \mathbf{E}(\mathbf{x}, \beta) \rangle = \mathbf{e}_j$, $\mathbf{e}_j$ is a unit vector in the jth direction, for some $j = 1, \ldots, d$, and $\langle \cdot \rangle$ means ensemble average over Ω or spatial average over all of $\mathbf{R}^d$. The effective complex permittivity tensor ϵ^* is defined as $\langle \mathbf{D} \rangle = \epsilon^* \langle \mathbf{E} \rangle$. For simplicity, we focus on one diagonal coefficient $\epsilon^* = \epsilon_{jj}^*$. The key result is an integral representation [4], [37] for $\epsilon*$ exploiting its Stieltjes properties as an analytic function of ϵ_1 / ϵ_2

$$F(s) = 1 - \frac{\epsilon*}{\epsilon_2} = \int_0^1 \frac{d\mu(z)}{s - z} \qquad (3.1)$$
$$s = (1 - \epsilon_1 / \epsilon_2)^{-1}$$

where μ is a positive measure on $[0, 1]$, determined exclusively from the geometry χ_1. In particular, μ is the spectral measure of the self-adjoint operator $\mathbf{\Gamma} \chi_1$, where $\mathbf{\Gamma} = \nabla(-\Delta)^{-1} \nabla \cdot$, $\Delta = \nabla^2$. Statistical assumptions about the geometry are incorporated into μ through its moments

$$\mu_n = \int_0^1 z^n d\mu(z) = (-1)^n \langle \chi_1 [(\mathbf{\Gamma} \chi_1)^n \mathbf{e}_j] \cdot \mathbf{e}_j \rangle \qquad (3.2)$$

with $\mu_0 = p_1$ if the volume fractions p_1 and $p_2 = 1 - p_1$ are known and $\mu_1 = p_1 p_2 / d$ if the material is statistically isotropic. In general, knowledge of the $(n+1)$-point correlation function of the medium allows calculation of μ_n (in principle).

Bounds on ϵ^*, or regions in the complex ϵ^*-plane in which the values of the effective complex permittivity must lie, are constructed from (3.1) by assuming partial knowledge of the moments of μ. For example, the region R_1 (the complex elementary bound) is obtained by assuming knowledge of only $\mu_0 = p_1$, while the region R_2 (the complex Hashin–Shtrikman bound) is obtained by assuming knowledge of $\mu_1 = p_1 p_2 / d$ as well. The deep relationship between the connectedness properties of a particular phase in the composite and the support of μ (where it is nonzero), in particular, the existence of a spectral gap around the endpoints zero and one, has been explored in [7], [39], and [41]. The spectral gap that exists for matrix-particle composites (a host material containing separated inclusions), like sea ice, which is cold enough, has

been exploited to derive tighter versions R_1^{mp} and R_2^{mp} of the complex bounds above. These bounds depend on a parameter q that measures the separation of the brine inclusions, and they are compared with C-band complex permittivity data [2] in [41, Fig. 2].

We now present a theorem that tells us when we can be assured that the microstructure, as characterized by μ, can be uniquely recovered [18]. This result can be viewed as a type of existence and uniqueness theorem for the inverse homogenization problem.

Theorem (Existence and Uniqueness for Microstructural Recovery): The measure μ in the integral representation (3.1) for the effective complex permittivity ϵ^* can be uniquely reconstructed if the values of ϵ^* are known along an arc in the complex s-plane.

For example, we may have a medium, such as sea ice, where the complex permittivity of at least one of the constituents, in particular, the brine, is dispersive. Then, as the frequency is varied, an arc is traced out in the complex s-plane (which could be a segment of the real axis). If measurements of ϵ^* are made all along this arc, the theorem tells us that μ can be uniquely reconstructed. However, this is an ill-posed problem that requires regularization to obtain a stable solution. The use of Tikhonov regularization [54] in the reconstruction of μ has been explored, yet it would also be interesting to examine the potential of applying causality, through the Kramers–Kronig relations, to stabilize the procedure.

In the above theorem, it is the measure μ that is uniquely reconstructed, yet it is the actual microstructure and its properties in which we are most interested. There arises the question of whether μ uniquely determines the microstructure or the stationary random field $\epsilon(\mathbf{x})$. Strictly speaking, the answer is no. For example, the expressions for ϵ^*, given in the Hashin–Shtrikman bounds in [41, Section III], can be attained by either a coated sphere geometry or a type of laminate geometry. Nevertheless, from an effective property point of view, these two "different" geometries are the same, in that they have the same effective property function $\epsilon^*(\epsilon_1/\epsilon_2)$. In particular, all the statistical properties of the two composites, such as volume fractions, isotropy, and all higher order correlation functions of the geometry, as measured by the moments of μ, are the same. Thus, the above theorem reconstructs the microstructure uniquely, up to the identification of composite geometries with the same effective complex permittivity functions, in the above way.

B. Inverse Bounds on Microstructural Parameters

We now describe how to invert the complex bounds R_1 and R_2 on ϵ^* to obtain rigorous bounds on the brine volume in sea ice from measurements of ϵ^*. The idea of the inversion is very simple, as follows. Given an observed complex permittivity value $\epsilon^*(n)$ from a set of N data points $n = 1, \ldots, N$ inside the bound R_1, as in [41, Fig. 2], we increase the brine volume fraction p_1 in the bound until one of the circular arcs on the boundary of R_1 touches this point, which defines the upper bound $Q_1(n)$ on the possible range of volume fractions associated with the data point. Similarly, we decrease

p_1 until the other arc touches the data point, giving a lower bound $P_1(n)$ on the possible range of brine volume fractions. Applying the same procedure to the isotropic complex bound R_2 yields even tighter lower $P_2(n)$ and upper $Q_2(n)$ bounds on the brine volume fraction p_1. Given a set of data points, we carry out the inversion for each point and then take the maximum over n of the $P_1(n)$ and the minimum over n of the $Q_1(n)$, and similarly for $P_2(n)$ and $Q_2(n)$, which yield rather tight, accurate estimates of the brine volume associated with the given data set. It should be remarked that a similar idea was used previously, at least to first order for R_1, and applied to multifrequency data for thin silver films [70]. Also, first-order analytical inverse bounds were derived in [20] and applied to geophysical mixtures in [95]. Other approaches to the inversion of microstructural information have been considered in [69] and [70].

We now make explicit the above outlined procedure. First recall that one arc of the region R_1 can be parametrized in the F-plane by

$$C_1(z) = \frac{p_1}{s - z}, \quad 0 \le z \le p_2. \tag{3.3}$$

The given, measured value of the complex permittivity $\epsilon^*(n)$ determines a corresponding value $F(n) = 1 - \epsilon^*(n)/\epsilon_2$. Assuming that the given value $F(n)$ lies on the lower boundary of the region R_1, by solving (3.3) for p_1, we obtain for the lower bound $P_1(n)$ on the brine volume fraction

$$P_1(n) = F(n)(s - z(n)). \tag{3.4}$$

It should be remarked that if the different measurements over n are made at different frequencies, then in general the value of s will also depend on n. Separating real and imaginary parts, we can immediately obtain

$$P_1(n) = |F(n)|^2 \frac{\operatorname{Im}(\bar{s})}{\operatorname{Im}(F(n))}, \quad z(n) = \frac{\operatorname{Im}(F(n)s)}{\operatorname{Im}(F(n))} \tag{3.5}$$

where the bar denotes complex conjugation. Note that our complex-valued data point $F(n)$ allows us to solve not only for the real brine volume fraction, but also for the real spectral parameter $z(n)$, which is associated with other details of the geometry, such as inclusion separation, and presumably forms a bound on the possible spectrum.

To obtain the upper bound $Q_1(n)$ on the brine volume, it is useful to turn to another auxiliary function [5] associated with the interchanged material, where ϵ_1 and ϵ_2 (as well as p_1 and p_2) are switched

$$J(u) = 1 - \epsilon^*/\epsilon_1 = \frac{1 - sF(s)}{1 - s}$$
$$u = (1 - \epsilon_2/\epsilon_1)^{-1} = 1 - s. \tag{3.6}$$

The advantage to using this function as opposed to $E(s)$ is that the spectrum [or support of μ in (3.1)] is trivially transformed via $u = 1 - s$, so that spectral bounds obtained for J are easily translated over to F, which is not the case for E. In the J-plane, the corresponding arc becomes

$$\tilde{C}_1(z) = \frac{p_2}{u - z}, \quad 0 \le z \le p_1. \tag{3.7}$$

Again assuming that the corresponding data point $J(n)$ lies on this arc, we obtain

$$Q_1(n) = 1 - |J(n)|^2 \frac{\operatorname{Im}(\bar{u})}{\operatorname{Im}(J(n))}$$
$$\tilde{z}(n) = \frac{\operatorname{Im}(J(n)u)}{\operatorname{Im}(J(n))}. \tag{3.8}$$

To obtain even tighter bounds on p_1 under the assumption that the microstructure is statistically isotropic, we apply the same inversion procedure to the complex bound R_2. Recalling that one arc of R_2 is given in the F-plane by

$$C_2(z) = \frac{p_1(s - z)}{s(s - z - p_2/d)}, \quad 0 \le z \le (d - 1)/d. \tag{3.9}$$

This arc gives an upper bound $Q_2(n)$ on p_1 defined by the corresponding analogue of (3.4)

$$Q_2(n)(s - z(n)) = F(n)s(s - z(n) - (1 - Q_2(n))/d). \tag{3.10}$$

Separating real and imaginary parts yields coupled, nonlinear equations for $Q_2(n)$ and $z(n)$. The resulting expressions are rather complicated and are omitted. We obtain the lower bound $P_2(n)$ on p_1 by applying the same procedure to the analogue of (3.9) in the J-plane, as above.

Finally, for a set of data points $\epsilon^*(n)$, $n = 1, \ldots, N$, we find that the intersection over n of the intervals $P_1(n) \le p_1 \le Q_1(n)$ for general media [20], given by

$$\max_n P_1(n) \le p_1 \le \min_n Q_1(n) \tag{3.11}$$

provides a good practical bound on the volume fraction p_1. For isotropic media, the intersection over n of the intervals $P_2(n) \le p_1 \le Q_2(n)$, given by

$$\max_n P_2(n) \le p_1 \le \min_n Q_2(n) \tag{3.12}$$

provides a very tight practical bound on the volume fraction p_1. In Fig. 6, we demonstrate our inverse bounds on the brine volume for a set of nine data points with frequency 4.75 GHz taken from [2]. The actual brine volume p_1 for the data is $p_1 = 0.02$. Complex permittivities of the ice and brine are calculated as described in [41, Section III]. The solid lines represent the intervals $P_1(n) \le p_1 \le Q_1(n)$ and $P_2(n) \le p_1 \le Q_2(n)$. The dotted lines represent the very tight prediction given by the inverse algorithm (3.12) for isotropic microstructures, which is in excellent agreement with the actual brine volume $p_1 = 0.02$.

Finally, we consider inversion of the matrix-particle bounds R_1^{mp} and R_2^{mp} to obtain inverse bounds on the microstructural parameter q, $0 \le q \le 1$, measuring the separation of the brine inclusions [77]. We consider a horizontal slice of sea ice (for the vertically incident waves of [2]) and assume that the brine is contained in separated, circular discs. Such an assumption allows us to use the exact calculations in [7] of the size of the spectral gap in the support of μ. In particular, we consider discs of brine of radius r_b, which hold random positions in a host of ice, in such a way that each disc of brine is surrounded by a "corona" of ice, with outer radius r_i. Then
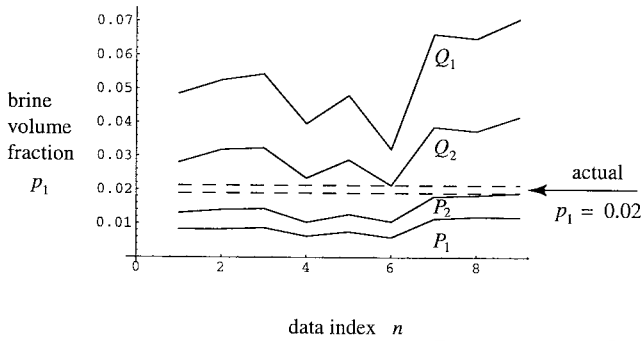
Fig. 6. Inverse bounds on the brine volume p_1 of sea ice derived from measured values of the complex permittivity $\epsilon^*(n), n = 1, \ldots, 9$, at 4.75 GHz. The solid lines represent the intervals $P_1(n) \leq p_1 \leq Q_1(n)$ for general media and $P_2(n) \leq p_1 \leq Q_2(n)$ for isotropic media. The dotted lines represent the very tight prediction given by the inverse algorithm (3.12) for isotropic media, which is in agreement with the actual brine volume $p_1 = 0.02$. For the data, the temperature $T = -11°C$, the salinity $S = 4.1$ ppt, and $\epsilon_1 = 42.2 + i45.6$ and $\epsilon_2 = 3.07$.

the minimal separation of brine inclusions is then $2(r_i - r_b)$. Such a medium is called a q-material, where $q = r_b/r_i$. For such a material, the matrix-particle bounds R_1^{mp} and R_2^{mp} [39], [41] assume the following form. The complex permittivity ϵ^* lies in the intersection of two circular discs, the boundaries of which are images of the real line $\mathbf{R}$ under different fractional linear transformations. With $p = p_1$, these circles have the form

$$F_{p,q}(z) = \frac{a(p,q)z + b(p,q)}{c(p,q)z + d(p,q)}, \quad -\infty \leq z \leq \infty \quad (3.13)$$

where the parameters of interest p and q enter the fractional linear transformation through the coefficients $a(p,q)$, $b(p,q)$, $c(p,q)$, and $d(p,q)$.

For observed complex permittivities, these forward bounds are inverted, yielding curves in (p,q)-parameter space. Such a curve is the locus of points $(\hat{p}, \hat{q})$ for which an observed ϵ^* lies on the circle $F_{\hat{p},\hat{q}}(\mathbf{R})$. Each observed value gives a different boundary curve. The resulting family of curves may be thought of as being parameterized by the observed complex permittivity. In all situations encountered for the forward bounds, the functional form of the coefficients $a(p,q)$, $b(p,q)$, $c(p,q)$, and $d(p,q)$ are polynomials in the two variables p and q. A general theorem is proved [77], stating that for such cases the inverse bound is a real algebraic curve $f(p,q) = 0$. This avoids having to solve coupled nonlinear equations that involve the spectral parameter z appearing in the argument of $F_{p,q}(z)$. As an example, under the assumption that the sea ice is a matrix particle composite, but without the assumption of statistical isotropy, the following polynomial is obtained:

$$f(p,q) = 2q^2 \text{Im}\Big\{ [2\epsilon^*(w + q^2)p + (\epsilon^* - \epsilon_2)(w^2 - q^4)]$$
$$\times \overline{[\epsilon^*(w + q^2) - \epsilon_2(w - q^2)]} \Big\}. \quad (3.14)$$

The bar denotes complex conjugation, and w is a constant, depending only on the complex permittivities of brine and pure ice $w = (\epsilon_2 + \epsilon_1)/(\epsilon_2 - \epsilon_1)$. The region of admissible (p,q) values is bounded by the real algebraic curve $f(p,q) = 0$.

Solving for p as an implicit function of q gives

$$p = \frac{1}{2} \frac{\text{Im}\left([(\epsilon^* - \epsilon_2)(w^2 - q^4)]\overline{[\epsilon^*(w + q^2) - \epsilon_2(w - q^2)]} \right)}{\text{Im}\left([\epsilon^*(w + q^2)][\overline{\epsilon^*(w + q^2) - \epsilon_2(w - q^2)}] \right)}. \quad (3.15)$$

Numerical calculation of the forward bounds using pairs of (p,q)-parameter values that lie in the acceptable region determined by the inversion algorithm yields consistent results. The essentially distinct algorithms used for computing forward and inverse bounds agree. Work on accurately reconstructing (p,q) pairs for actual data sets is ongoing.

IV. INVERSE SCATTERING ALGORITHMS FOR THE RECOVERY OF SEA ICE THICKNESS

In this section, we consider a variety of methods for inverting electromagnetic scattering data for sea ice thickness. The recovery of thickness information is one of the central challenges of sea remote sensing. The algorithms presented below, along with the methods of Section II, provide a foundation for meeting this challenge.

A. Radiative Transfer—Thermodynamic Inverse Model for Thickness Retrieval from Time-Series Scattering Data

Sea ice thickness is an important factor in understanding the dynamics of sea ice cover as well as the air–ocean heat exchange. Although spaceborne SAR images have been successfully applied in mapping the extent and identifying the types of sea ice [59], the direct use of simple empirical models, based on the SAR measurements, for sea ice thickness retrieval is still limited because of the complex interactions of electromagnetic waves with the dynamically varying sea ice medium. Also, it becomes too difficult to derive analytic inverse solutions from direct scattering models of sea ice [25], [34], [72], [97], [98], [107] for the ice thickness. To utilize such developed scattering models, the parametric estimation method can offer a greater flexibility in the choice of forward models, the parameters to be inverted, and the data to be employed [52]. However, such an approach usually has associated problems of nonunique solutions and inversion stability with noisy data. Although it might be possible to reduce the effects of these uncertainties by using diversified multifrequency, multiangle, and polarimetric data, the cost of such extensive measurements may be prohibitive for satellite remote sensing of sea ice. On the other hand, orbiting satellites repeat their passes at a fixed time interval; it is natural for them to make timely sequential observations. With these time-series measurements, more data become available, which is helpful in resolving the nonuniqueness and stability problems and useful for the geophysical parameter reconstruction.

Recently, ice-thickness reconstruction algorithms based on the combined use of sea ice electromagnetic scattering models, time-series remote-sensing data, and a parametric estimation technique have been developed [52], [86], [87], [99], [100]. Veysoglu et al. [99], [100] have developed an inversion algorithm using passive microwave measurements of sea ice. They have shown that, by incorporating a Stefan's growth
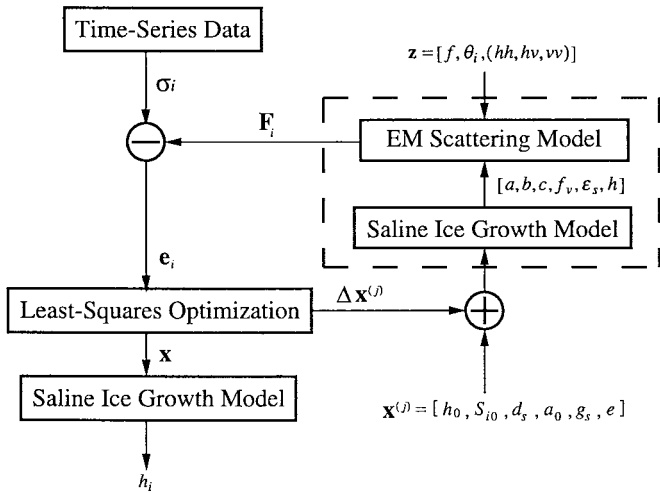
Fig. 7. Block diagram of the radiative transfer—thermodynamic inversion algorithm using time-series measured data. The dynamic electromagnetic scattering model, which includes the electromagnetic scattering model and the ice growth model, is enclosed by a dashed rectangle.

model [9] into the sea ice inverse scattering problem, the thickness estimation can be constrained sufficiently to predict more accurately the evolution of sea ice growth. The inversion scheme is based on nonlinear optimization using the Levenberg–Marquardt method [65]. Shih et al. [86], [87], from the experimental observations and the thermophysics of ice growth, developed a retrieval algorithm for ice thickness based on a dynamic electromagnetic scattering model of saline ice and time-series active remote-sensing data. This inversion algorithm using active radar measurements is summarized in Fig. 7.

In this algorithm, the growth model for saline ice consists of the following set of equations:

$$\frac{dh}{dt} = \frac{1}{\rho L} \frac{T_m - T_a}{\frac{1}{e} + \frac{h}{\kappa_i}} \qquad (4.1)$$

$$S_i = S_{i0} - d_s h \qquad (4.2)$$

$$a = a_0 + g_s h. \qquad (4.3)$$

The estimation of the growth of ice thickness is given by (4.1), which is a heat and mass balance equation [53], [104], where h is the ice thickness, $\frac{dh}{dt}$ is the growth rate, T_a is the air temperature, and T_m is the ice melting temperature, where all temperatures are in °C. The thermal conductivity of saline ice in W/m/°C is κ_i, L is the latent heat of freezing in J/kg, the quantity e is the heat transfer coefficient between ice and air, which accounts for contributions from both convection and radiation, and ρ is the density of the ice. The growth of sea ice also accompanies the desalination process [26], and (4.2) approximates the reduction of the bulk salinity, S_i in $^0/_{00}$, of thin saline ice by a monotonic decreasing function of ice layer thickness h and a desalination factor d_s. Equation (4.3) describes the change of brine inclusion size a with the ice thickness h and a size expansion factor g_s. This assumption has been tested by comparing the theoretical model results with the experimental data on radar backscatter signatures [73], [86], [87]. From these equations, the state of the ice at a certain stage can be estimated from previous states. With

electromagnetic measurements made in a time series, it is helpful to use these correlations to improve the retrieval of relevant physical parameters.

The radiative transfer scattering model of sea ice [25], [86], [87] described in [41, Section V] is used in this algorithm to provide a relationship between the expected backscatter measurements to the radar parameters and the saline ice characteristics. This relationship can be expressed as

$$\sigma_i = \mathbf{F}(t_i, \mathbf{z}, \mathbf{x}) + \mathbf{e}_i \qquad (4.4)$$

where σ_i is the measurement data vector whose elements consist of backscattering coefficients, $\mathbf{F}(t_i, \mathbf{z}, \mathbf{x})$ is the model response, and $\mathbf{e}_i$ represents the discrepancy between the observation and the model result. The index i is used to denote the measurement time at t_i. The array $\mathbf{z}$ denotes the set of known radar parameters, such as the frequency f, polarization, and looking direction. The vector $\mathbf{x}$ contains the pertinent model parameters of saline ice

$$\mathbf{x} = [h_0, S_{i0}, d_s, a_0, g_s, e] \qquad (4.5)$$

where $h_0 = h(t_0)$ is the ice layer thickness at time t_0 at which the reference time for the first set of data is taken. The other parameters S_{i0}, d_s, a_0, g_s, and e have been defined in (4.1)–(4.3). (The notation $\mathbf{x}$ and $\mathbf{e}_i$ should not be confused with the different meanings used above.)

In the retrieval analysis, the model parameters $\mathbf{x}$ are to be reconstructed from the scattering data. The approach is to measure the data σ and invert the relation (4.4), i.e., to express the parameter x_j in terms of σ. The minimization of the sum of squares of the difference between the measured data and the model response is performed by using the Levenberg–Marquardt algorithm [65]. [This method is a hybrid of the steepest descent (SD) method and the inverse Hessian method. When initial parameters give a solution far from a minimum, the SD method is used to get close to the minimum, the problem is assumed to become quadratically convergent, and the inverse Hessian method is employed to further converge to the solution within the specified accuracy. During the parameter adjusting process the Levenberg–Marquardt method blends or varies smoothly between these two methods.] At the j-th iterative step in Fig. 7, the vector of estimated parameters $\mathbf{x}^{(j)}$ consists of ice parameters at a specific time, including the initial ice thickness, initial salinity, initial brine pocket size, desalination factor, brine size growth factor, and the heat transfer coefficient. (In this figure, a, b, and c denote the dimensions of the brine inclusions in the three principal directions, f_v denotes the volume fractions of the inclusions, and ϵ_s denotes the permittivity of the sea ice.) The subsequent thicknesses, salinity, and brine pocket sizes at different growth stages are calculated according to the saline ice growth model described in (4.1)–(4.3) and the elapsed time between each measurement. This set of ice parameters is then substituted into the electromagnetic scattering model, which solves the radiative transfer equation and generates a simulated time series of backscattering coefficients that is compared with the vector of measurement data. Thus, the object function contains the whole time-series measured and model data, in contrast to
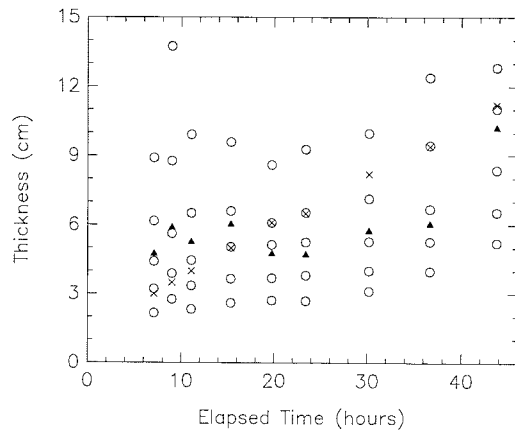
Fig. 8. Thickness retrieval without time-series information. The circles show possible combinations of thickness, brine pocket size, and brine volume, which may give similar backscattering coefficients at a specific time. Filled triangles represent inversion results without time-series information. The ground truth of ice thickness is represented in cross.

TABLE I
INITIAL GUESSES, CONSTRAINTS, AND INVERTED MODEL PARAMETERS FOR THE RADIATIVE-TRANSFER THERMODYNAMIC INVERSE MODEL

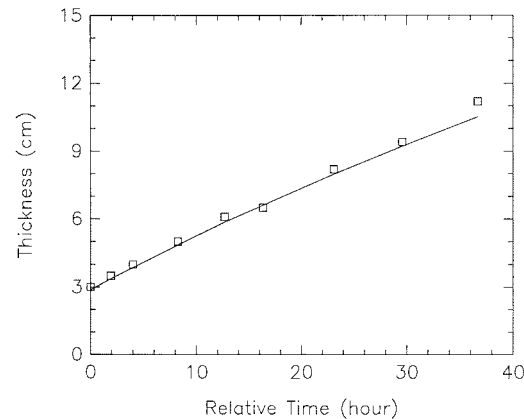| model parameters	initial guess	lower limit	upper limit	final value	
				25°	30°
h_0 (cm)	1.00	1.00	8.00	2.87	3.58
a_0 (cm)	0.0120	0.0120	0.0150	0.0128	0.0121
g_s	0.00200	0.00150	0.00200	0.00169	0.00163
S_{i0} ($^0/_{00}$)	20.0	15.0	20.0	15.6	15.1
d_s ($^0/_{00}$/cm)	0.50	0.50	0.80	0.50	0.54
$e(W/m^2/^\circ C)$	10.0	8.0	12.0	8.0	8.0

Fig. 9. Thickness retrieval with polarimetric time-series data. The boxes represent the measured ice thicknesses. The solid curve indicates the evolution of reconstructed ice thickness using measured time-series data at 25° incident angle.

the data at one specific time. If the model data do not agree with the measured data, the model parameters are adjusted. To minimize the least-squares object function, the entire series of simulation and experimental results must be matched. In this way, the range of possible retrieved thicknesses from an initial trial thickness can be reduced and the retrieval may be robust to the discrepancy between model responses and measurements. The procedure is then repeated until the error threshold is reached. The inverted initial thickness is finally applied back to (4.1) to reconstruct the ice thickness for the entire growth stage. This inversion algorithm was applied to retrieve the growth of a sheet of thin saline ice by using the set of C-band polarimetric radar sequential measurements from the CRRELEX'93 experiment. The experiment is detailed in [73].

We first consider the thickness retrieval without incorporating the time-series information. For this case, each 25° incident angle data set [73], [86], [87] at a specific time is inverted separately. The open circles shown in Fig. 8 indicate the possible solutions of thickness corresponding to the backscatter at that specific time, while the cross symbols represent the measured thickness. This ambiguity in the thickness retrieval is to be expected since different combinations of thickness, brine volume, and brine pocket size may give a similar backscattering coefficient, i.e., the electromagnetic scattering model alone does not provide sufficient information to reconstruct the ice thickness uniquely. We further reduce the number of unknowns to let the thickness be the only unknown model parameter, the same set of backscatter data at 25° incident angle is applied to invert ice thickness. The retrieved thickness, as denoted by the filled triangles in Fig. 8, still shows large fluctuations from the measured ground truth, which is caused by some measurement uncertainties and the inaccuracy of simplified saline ice scattering model. This example demonstrates an unsuccessful inversion even with only thickness being the unknown parameter.

To avoid the nonuniqueness and noise problems, the inversion with time-series measured data is considered next. The initial thickness is the pertinent parameter to be inverted. Since

the growth rate of ice is not *a priori* information, the heat transfer coefficient e is also included as an unknown model parameter. The unknown model parameters are constrained within appropriate physical ranges instead of letting all parameters vary freely, which will cause the inversion algorithm inefficient as well as susceptible to some local minimum attractions or divergences. Table I gives the initial guesses, constraints, and the inverted values of model parameters for this inversion. The constraints on model parameters S_{i0}, d_s, and e are determined by referencing the measured ground truth and the findings in published literature. On the other hand, the model parameters a_0 and g_s are determined based on the forward model simulations and allowed a ±15% variation range. The reconstructed ice thicknesses are shown in Figs. 9 and 10 for two different incident angles 25 and 30°, respectively. It is noted that the retrieved ice thickness obtained by using this time-series inversion algorithm agrees very well with the measured ice growth. The retrieved thickness for the 25° data set appears better than the one for 30°, which may be due to the larger deviation between model simulation and measured data in cross polarization at the 30° incident angle [73], [86], [87].

In summary, an accurate inversion algorithm for the thickness of thin saline ice has been developed based on the electromagnetic scattering model, ice growth physics, and parametric estimation method. Time-series measured data were
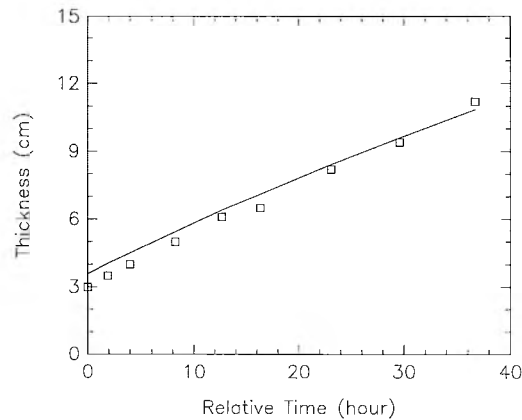
Fig. 10. Thickness retrieval with polarimetric time-series data. The boxes represent the measured ice thicknesses. The solid curve indicates the evolution of reconstructed ice thickness using measured time-series data at 30° incident angle.

used instead of multifrequency or multiangle data to reduce the effects of uncertainty and noise. The saline ice growth model provides more information to constrain the parametric estimation method. As a result, a better retrieval of thickness is achieved by utilizing these time-series measurements in this method. The demonstrated accuracy of the thickness retrieval suggests the potential use of this algorithm for retrieving geophysical parameters from time-series satellite remote-sensing data. The inversion algorithm is recently applied to the case of ice growth under diurnal variations. Comparisons with experiment for such cases will be reported shortly.

B. Neural Network Inversion for Sea Ice Thickness

In general, the inversion of geophysical parameters is complex because of the multidimensionality, the interrelationship, the dynamics, and the physical interactions under different environmental conditions. In this respect, neural networks are particularly suitable because of their ability to adapt to the geophysical multidimensionality and their robustness to noise in realistic remote sensors. Neural networks have been studied intensively [60] and have found remote-sensing applications in snow parameter retrieval with passive microwave data [96] and particle size determination with optical data [51] for instance.

In this section, we demonstrate the use of neural networks to invert for thickness of young sea ice with multifrequency polarimetric microwave data. The approach is to retrieve the ice thickness by using the analytic wave theory model [72] described in [41] to train the neural network to match measured data in the selection of the ice thickness. There are several types of networks, such as the Hopfield net, the Hamming net, and the Kohonen self-organizing feature mapping. Here, we use the multilayer perceptron with a modified backpropagation algorithm to improve the convergence rate and accuracy [49]. Interrelations of physical parameters governed by sea ice physics under typical Arctic winter environmental conditions are utilized to restrict the solution space to avoid extraneous solutions and shorten the required computation time.

The C-band and L-band polarimetric SAR data used in this study were collected in March 1988 by the Jet Propulsion Laboratory, Pasadena, CA, SAR onboard the NASA/DC-8 aircraft during the Beaufort Sea Flight Campaign [10] over a sea ice experimental area, located near 75° N latitude and spanned 140–145° W longitude. Each frequency channel has the capability of simultaneously collecting linear like-polarized (HH and VV) and cross-polarized (HV and VH) backscatter data. The transmitter alternately drives the HH- and VV-polarized antennas, while dual receivers simultaneously record the like-polarized and cross-polarized echoes. In this manner, the scattering matrix of every resolution element in an image is measured. The spatial resolution of the four-look SAR data used here is approximately 6.6 and 11 m in the slant range and azimuth directions, respectively. The range of look angles is between 20 and 70°.

In the Beaufort Sea experiment region, ice conditions comprised a mixture of first-year and multiyear ice forms in this region of transition between the polar pack and younger near shore ice [30]. High ice drift speeds experienced during the experiment [106] create newly opened and refrozen leads and offer the opportunity to acquire airborne radar data for young ice over a large range of incident angles. Note that surface-based data of young thin ice are scarce due to its inaccessibility and fragility in the natural environment. Although we do not have direct surface measurements of the thickness, the evidence of the thickness range of the ice is given by the weather and ice conditions acquired by the Applied Physics Laboratory Ice Station (APLIS), University of Washington, Seattle, in the experimental area [106] and the almost contemporaneous high-resolution passive microwave observations. The passive microwave observations were acquired by the Naval Research Laboratory (previously NORDA), Washington, DC, Ka-band scanning radiometer system (KRMS) [32]. Ice properties, including salinity, temperature, brine inclusions, and surface roughness, have been presented [58].

The neural network as a nonlinear estimator is used for retrieving the mean thickness for the young ice. The scattering model [58] is used to generate the polarimetric scattering coefficients of sea ice with a range of thickness between 0 and 15 cm at the C- and L-band. The five polarimetric coefficients used here are σ_{HH}, σ_{HV}, σ_{VV}, $\text{Re}(\sigma_{hhvv})$, and $\text{Im}(\sigma_{hhvv})$. This data set provides the input–output pairs to "train" the neural network such that the resultant network would provide an estimate of the thickness when presented with a set of polarimetric scattering coefficients. The neural network employed in this study consists of an input layer, an output layer, and two hidden layers with the nodes in each layer connected to each other. The number of input nodes for the input layer equals the number of input elements. In this case, the inputs are the five polarimetric backscatter coefficients. The number of nodes in the second and third layer are 10 and 30, respectively. There is only one output node since the average ice properties are functions of ice thickness, which provides an estimate of the thickness of the ice given the polarimetric observations.

Fig. 11 shows the overall thickness results of young sea ice in the refrozen new leads over the incident angle range, where
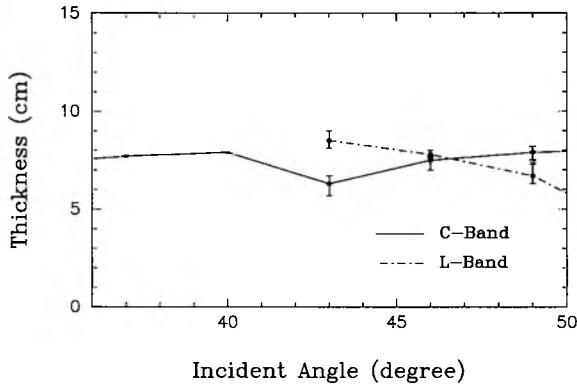
Fig. 11. Comparison of theoretical predictions of ice thickness from neural network inversion with data taken in the Beaufort Sea.

data are available. The near range incidence angles (less than 35°) are not shown here because some of the radar data are saturated in this range and saturated the network. At both C- and L-bands, the estimated average thickness of the lead ice is between 6 and 9 cm, which shows consistency in the process. Fig. 11 also shows errors caused by ± 1-dB uncertainty in the radar measurements or model calculations in the incident angle range common to C- and L-bands. This work has illustrated the use of neural network in retrieving sea ice thickness from polarimetric microwave SAR data with noise.

C. Reflectivity Inversion for Sea Ice Thickness

In most of the studies in the past on the use of active measurements [35], [58], [86], backscattering coefficients have been used for retrieving thin saline ice thickness. It is known that there are a few decibels of fluctuation in these types of data, and hence, statistical methods, such as the neural networks, have been used for retrieval. Fluctuations are resolved by the use of multiple inputs in terms of frequency, polarization, and/or the incident angle and their known relative values. Clearly, a data set with much less fluctuations will provide even better results in identifying ice thickness and may allow a simple and more direct retrieval in some cases.

In this section, we consider the relations between ice thickness and both the coherent and incoherent reflectivity properties of a layer of saline ice over saline water. It is shown that a new incoherent reflectivity along with the standard coherent reflectivity are needed to explain reflectivity measurements. Physically, it is clear that when the ice is less than or comparable to the incident wavelength, the transmitted and reflected fields within the ice interfere coherently. This is true when the ice thickness is about a wavelength or less in ice. When the ice gets thicker, the lower interface gets rougher and loss gets higher, the coherency between the transmitted and reflected field is lost and the reflectivities of VV- and HH-polarizations become incoherent. The transition takes place between one and two wavelengths. Measurements of reflectivity taken over two wavelengths in ice follow incoherent reflectivity behavior quite well.

For a continuous incident wave, the impedance seen by it at the air–ice boundary is the total field impedance accounting

for both the ice layer and the water below it. It is known that the field reflection coefficient for such a layer is given by

$$R_c(\theta, d) = \frac{R_1 + R_2 e^{-2(\alpha + i\beta)d}}{1 + R_1 R_2 e^{-2(\alpha + i\beta)d}} \qquad (4.6)$$

where $\alpha = \mathrm{Re}[ik(\epsilon_r - \sin^2\theta)^{1/2}]$; $\beta = \mathrm{Im}[ik(\epsilon_r - \sin^2\theta)^{1/2}]$; R_1, R_2 are the Fresnel reflection coefficients at the air–ice and ice–water interfaces, respectively; θ is the incident angle, and d is the thickness of the ice layer. The coherent reflectivity is given by

$$\Gamma_c = |R_c(\theta, d)|^2. \qquad (4.7)$$

An incoherent reflectivity was given by Ulaby et al. [98] as

$$\Gamma_i(\theta, d) = \frac{\Gamma_1 + \Gamma_2(1 - 2\Gamma_1)e^{-4\alpha d \sec\theta}}{1 - \Gamma_1\Gamma_2 e^{-4\alpha d \sec\theta}}. \qquad (4.8)$$

However, it is found that an expression that fits the measurement better is

$$\Gamma_{\mathrm{in}} = |R_i(\theta, d)|^2 \qquad (4.9)$$

where

$$R_i(\theta, d) = \frac{R_1 + R_2 e^{-2\alpha \sec\theta d}}{1 + R_1 R_2 e^{-2\alpha \sec\theta d}}. \qquad (4.10)$$

1) Surface Backscattering Model Approach: A surface backscattering model was used in [35] to explain backscattering from the saline ice layer. It was found that surface scattering was responding to the total effective permittivity of the ice layer and the water beneath it. It is clear that, when the water below is not seen by the radar, only the permittivity of ice will be in effect. Otherwise, an effective total permittivity for the combination of the ice layer and water is sensed. It is this property that allows the ice thickness to be calculated at a given wavelength. Note that the conventional idea of a perfectly plane layer in which we can expect two echoes from the top and bottom ice interfaces is not applicable here because the ice–water interface may be rough and the echo may be diffused and difficult to detect. In the next subsection, we shall see that this idea is supported by reflectivity measurements.

It is known that when the ice surface is randomly rough, many samples are required to reach the statistical average. Thus, generally, there is some fluctuation in the data. In Fig. 12, we show a comparison between backscattering calculations at 5.3 GHz and data plotted versus ice layer thickness at 25 and 40° incidence using the integral equation surface scattering model [34]. The coherent reflection coefficient due to a layer is used for ice thickness up to 2 cm, beyond which we use the effective permittivity inverted from the incoherent reflectivity to calculate backscattering. The permittivity of the saline ice is taken to be 3.4-i0.2. The permittivity of the saline water is computed based on the formula given in [98] at -5 °C. The correlation function of the surface is taken to be exponential, and its rms height and correlation length are taken to be 0.08 and 0.8 cm, respectively. While there is an overall agreement, a deviation of a few decibels between model predictions and data are evident. Similar deviations between model predictions and data are also evident in [58] and [86].
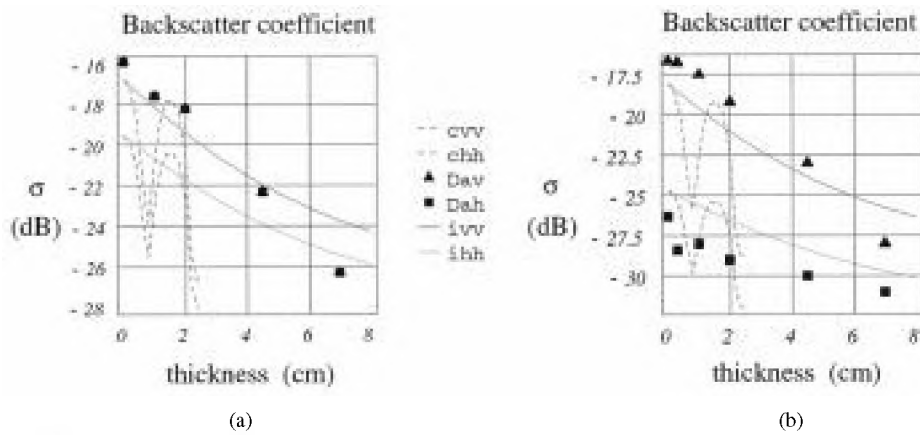
Fig. 12. Comparisons between surface-scattering model and data for VV- and HH-polarizations at 5.3 GHz (a) 25° and (b) 40°, respectively, where c denotes coherent scattering, D denotes data, and i denotes incoherent scattering.
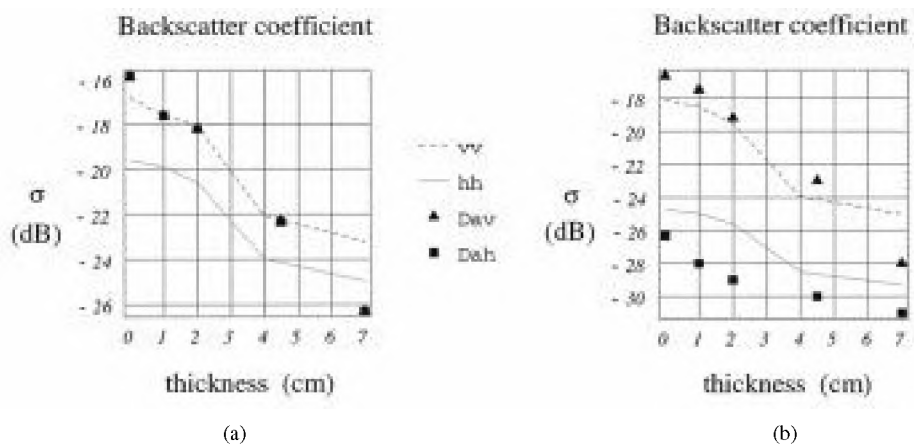

Fig. 13. Comparison between model and data using measured permittivity as input at 5.3 GHz for VV- and HH-polarization and incidence angle of (a) 25° and (b) 40°, respectively.
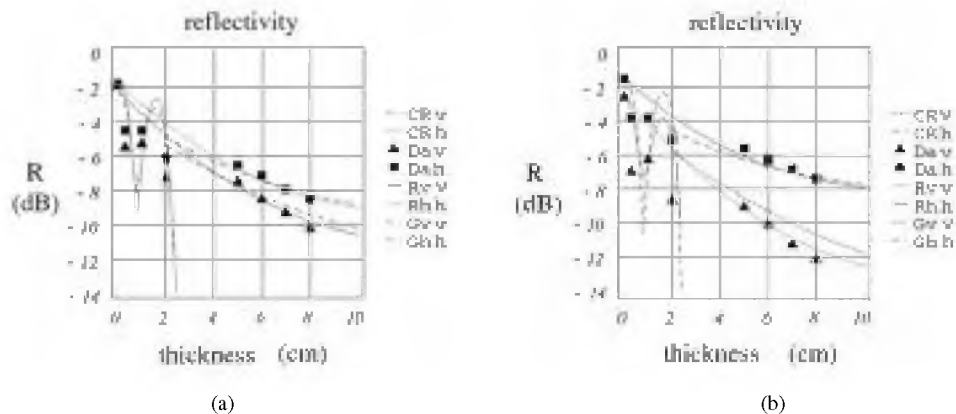

Fig. 14. Comparisons of coherent and incoherent reflectivity model results with measurements at incidence angles of (a) 25° and (b) 40°. C denotes coherent reflectivity, R denotes incoherent reflectivity in (4.9), and G denotes the reflectivity in (4.8).

If instead of theoretical estimates of reflectivity we use the permittivity inverted from measured reflectivity in the surface scattering model, we obtain better agreement at 25° incidence but no significant improvement at 40° incidence, as shown in Fig. 13. For this reason, a direct retrieval of ice thickness is not feasible. A statistical method, such as a neural network, could be used [58].

2) Ice Thickness Retrieval: Reflectivity measurements were carried out over saline ice at 25 and 40° incidence and 5.3 GHz. In Fig. 14, comparisons are shown between measured data and the coherent and incoherent reflectivities given by (4.7)–(4.9) as a function of ice layer thickness. Of the two incoherent reflectivity models, it is seen that (4.9) gives a better fit to the data than (4.8). More importantly,

there is very little data fluctuation after the ice thickness is larger than 4 cm. It appears that, when the ice thickness is less than or around one wavelength, the wave transmitted into the ice interferes coherently with the field reflected from the ice–water interface. Thus, we can only interpret the data using a coherent reflectivity model given by (4.7). After about 4 cm (which is about two wavelength in thickness), the waves become incoherent and a specific trend appears, as shown in Fig. 14. This specific data trend is much clearer and more stable than what can be obtained from the backscattering measurements shown in the previous subsection. It appears that ice thickness can be inverted directly from reflectivity measurements when the thickness is over one wavelength.

D. Proxy Indicators of Sea Ice Thickness

Faced with the difficulties of determining sea ice thickness through electromagnetic means, people have developed alternatives to direct thickness measurements, one of these being the use of proxy indicators. A remotely sensed proxy indicator of sea ice thickness is a characteristic, physical property, or suite of physical properties that is tied to ice thickness and has a measurable electromagnetic signature. To date, the most successful general proxy indicator of ice thickness that can be determined through remote sensing has been ice type or age [8], [57], [59], [103] First-year ice (ice that is less than a year old) is in general thinner than multiyear ice (ice that has survived one or more melt seasons). The age of sea ice is manifested by a suite of physical properties, such as brine pocket size and brine distribution, that affect scattering and emission of radiation. A separation between first-year and multiyear ice, however, only gives rough information about ice thickness.

For thin sea ice, proxy indicators other than ice type have recently been investigated. In the microwave, experiments and models have indicated that electromagnetic signatures of new sea ice are tied to surface roughness and dielectric properties [3], [29], [89], [91], [101]. Through modeling, Zabel et al. [113] looked into the competition between the influence of near-surface dielectric changes and surface roughness changes on the microwave backscatter of young, growing sea ice. They found that surface roughness changes tend to dominate over dielectric changes after the initial 10 cm of ice growth. Unfortunately, surface roughness is not a reliable proxy indicator of ice thickness because it can change rapidly due to events, such as snowfall and ridging. A more reliable, though transient, event may be the growth of frost flowers, which typically happens while the ice is about 5–20 cm thick and results in strong microwave backscatter. Zabel et al. [113] also hypothesized that the surface dielectric constant of sea ice may serve as a proxy indicator for young sea ice thickness when using microwave sensors operating at an incidence angle of about 12°. At this angle, experiments showed that the microwave backscatter is largely insensitive to surface roughness.

Another proxy indicator for thin sea ice thickness is ice surface temperature. The basic idea is that the surface temperature of thin ice tends to be higher than that of thick ice. This ten-

dency is observed in infrared imagery [44], [66], [112]. Using thermal infrared imagery and a thermodynamic model for ice growth, Yu and Rothrock [112] have demonstrated calculations of thin sea ice thickness distributions largely to within 2% of sonar-based distributions (sonar is considered the most reliable remote-sensing tool for measuring ice thickness). The largest difference between the two distributions (20%) occurs for very thin ice. For ice thickness itself, they report an uncertainty in their method of roughly half the ice thickness. Infrared methods suffer by comparison to microwave methods in that infrared sensors are limited by cloud cover. Nevertheless, ice surface temperature appears to be a useful proxy indicator for sea ice thickness.

V. NEURAL NETWORK CLASSIFICATION OF SEA ICE TYPE

The purpose of this section is to introduce a classification scheme for sea ice types based on a special neural network known as the fast-learning neural network [63], [28]. Learning in a neural network can be viewed as minimizing the sum of the squared errors between the desired outputs and the computed network outputs by adjusting the weights inside the network. One problem with the conventional backpropagation neural network learning method is that the resultant error is highly dependent on the initial weights [83] and may not find the global minimum of the error function. The fast-learning algorithm has been shown to be much less sensitive to this problem [27]. The Fast-learning method differs from the backpropagation in that the output of the fast-learning neural network is expressed as a linear function of the output weights, and linear equations can be solved exactly to minimize the training error. The basis functions of these linear equations are the sigmoid activations commonly found in neural networks. The advantages of the fast-learning neural network over the backpropagation neural network for a sea ice classification problem are demonstrated in this section.

When considering training data for neural networks to perform classification, it is necessary that the training data fully represent all of the domain of the input set rather than primarily the means, as in a k-means classification. This is due to the fact that the neural network needs to know where to position the discrimination planes in n-dimensional space. The performance of a neural network in classification problems is more dependent on having representative training samples, whereas the statistical classifiers need to have an appropriate distribution model for each class. This is an important difference between the neural network and conventional statistical classification.

A large amount of data currently available to the remote-sensing community originate from aircraft and satellite-based platforms. These data usually have little or no ground-truth information that would allow them to serve as training data, as required in a supervised classification scheme. Although the unsupervised classifiers or clustering algorithms can group data into logical sets that have similar features, these classifiers do not identify what specific ice type each cluster represents. A possible method to identify the ice type associated with a cluster is to compare it with clusters from known ice types,

TABLE II
SUMMARY OF RADIOMETRIC AVERAGES FOR THE EIGHT CLASSES CONSIDERED. ALL VALUES GIVEN ARE IN KELVIN

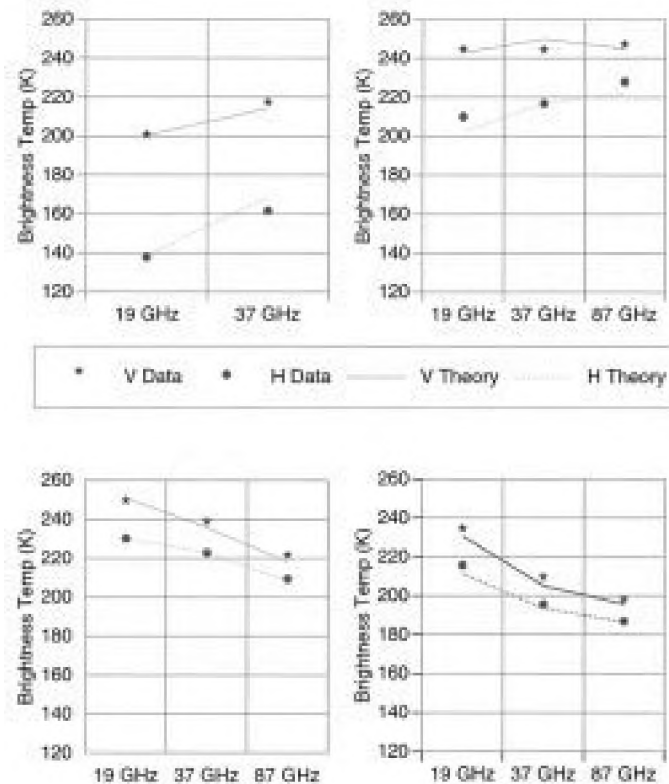| Channel	Open	Frazil Ice Water	Thin Ice	FY	2nd Year	Inter. (mix)	MY	Old MY
19V	197.6	241.5	252.6	246.7	239.7	234	231.6	223.7
22V	206.1	241.8	251	244.2	236.3	229.6	226.4	217.7
37V	214.5	241.4	247.4	235.8	223.7	216.2	206.7	195.9
85V	240.9	244	237.1	218.7	210.8	208.7	195.1	193.1
19H	136.5	208.6	233.6	228.7	220.7	214.5	214.4	206.4
37H	160.3	215.5	232.5	221.4	208.8	199.4	194.3	183.7
85H	203.6	226.7	225.9	207.9	199.8	197.2	185.6	183.5

Fig. 15. Identification of unsupervised classification cluster centroids using an emission model from [34].

which serve as ground truth. If only the mean radiometric values of ice types are available, another method is to use a validated scattering or emission model. The model should produce the mean value, when the model parameters take on their mean values for a given ice type. Variations of the model parameters about their mean values should allow the model to generate the cluster. Thus, a physical emission model calibrated by a data set from a known ice type may be used to identify a cluster of the same ice type. To illustrate the classification method with a fast-learning neural network, we shall consider a specific example using radiometric data from the spaceborne SSM/I platform.

1) Classification Example: The SSM/I is a seven-channel, four-frequency, linearly polarized, passive microwave radiometer system [47], [80]. The instrument measures surface brightness temperatures at 19.3, 22.2, 37.9, and 85.5 GHz. All data are at 53° from nadir. Data from March 1–15, 1988, are processed to remove outliers. The data are then clustered

into eight classes using an unsupervised ISODATA algorithm [79] These eight classes of ice can be identified with either clusters of radiometric measurements from known ice types acquired from radiometric images [27] or using a calibrated emission model. An emission model can be calibrated with any emission data representative of known ice types. A sufficient number of such data sets are difficult to find. To illustrate this approach, an emission model based on the radiative transfer method [34] is used to fit centroids already established by [23]. The centroids of the ice categories used are given in Table II. An example of model calibration is shown in Fig. 15 for open water, frazil ice, first-year ice, and multiyear ice. Once the calibration process is complete, we can apply this calibrated model to determine the ice types represented by the eight clusters found using unsupervised clustering.

After the original image is classified using the unsupervised method and the identity of each class is known, the final classified image can be used as pseudoground truth for a
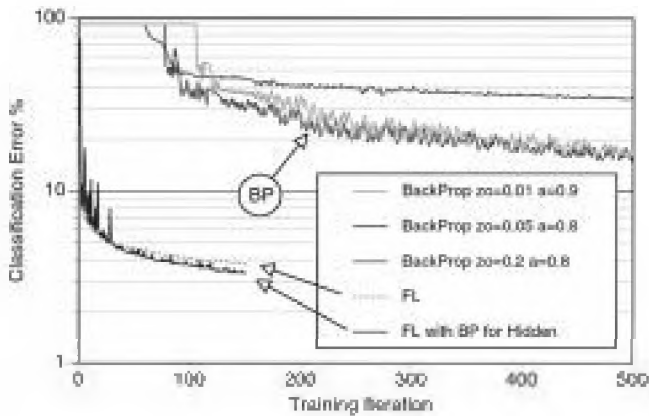
Fig. 16. Comparison of training classification error as a function of iteration for the five cases listed. The training set contained 30512 patterns. All networks used the same fully connected 7-15-8-8 topology.

TABLE III
COMPARISON OF TRAINING TIME, ITERATIONS, ERROR USING 7-15-8-8 TOPOLOGY—(THERE WERE 30512 PATTERNS IN THE CLASSIFICATION TRAINING FILE)

Job Name	Time Required	Iterations	Avg Time(sec) /Iteration	Min Error%
BP-18522	19558.8	500	39.12	16.76
BP-18513	19526.9	500	39.05	14.86
BP-18494	19521.07	500	39.04	34.51
FL	4478.3	150	29.85	3.805
FL+BP	6736.9	150	44.91	3.382

supervised neural network classification scheme. Representative data from each of these eight classes and an associated class identification tag are dumped to a file and used to train a neural network. The trained neural network classifier can then be used for batch processing satellite or aircraft data. For the example considered, the neural network will need to have seven inputs (one for each radiometric channel) and eight outputs (one binary output for each class). From experience with similar data, two hidden layers with 15 and 8 units, respectively, are used in the neural network. This four-layer network is commonly denoted by 7-15-8-8. A conventional backpropagation learning algorithm and the fast-learning algorithm are used to train the neural network. The primary difference between the fast-learning method and the backpropagation method is that the fast-learning method finds the global minimum of the error function with respect to output weights, not with respect to all weights within the network as the backpropagation method does. The fast-learning method is optimizing the output weights rather than all hidden weights as required by the backpropagation algorithm. In addition to these two methods, a third hybrid method combining fast-learning and backpropagation is also used (fast-learning + backpropagation). After solving for the output weights as performed by the fast-learning method, the combined fast-learning + backpropagation method uses backpropagation to correct the hidden weights.

Results: All three algorithms (backpropagation, fast-learning, and fast-learning + backpropagation) were tested on the same training file using the same 7-15-8-8 fully interconnected topology. The training set consisted of 30512 training patterns. Three separate attempts to train the network using backpropagation were made; each with different learning rates and momentum factors [83]. The time required for training the network, the final classification error, and the number of iterations required are given in Table III. The classification error during training for all methods is plotted as a function of epoch in Fig. 16.

From Table III, we see that the backpropagation training algorithm did very poorly in comparison to the fast-learning algorithms. Note that even in cases in which backpropagation

was allowed to run three times as long as fast-learning, the backpropagation training error is a full magnitude greater. Although the combined fast-learning + backpropagation did slightly better than fast-learning alone, the additional training time required may not be justified. Thus, the fast-learning is the method of choice for this problem. The fast-learning + backpropagation classified image is shown in Fig. 17(b) along with the results of the NASA Team Algorithm (NTA) [90] in Fig. 17(a). This figure provides a qualitative comparison of multiyear concentration from NTA with the ice ages estimated using the fast-learning + backpropagation approach described here. Note the general agreement in shape, especially in the Fram Strait (north of Svalbard) labeled "p1" and the region just north of Ellesmere Island (labeled "p2").

In summary, a validated emission model can be combined with other techniques, such as the fast-learning + backpropagation neural network, to effectively perform classification for complex problems, such as sea ice. In this example, we used a clustering algorithm that is better suited for data without ground truth and then applied an emission model to determine class identity. This approach allows us to use the results of the clustering algorithm to train a neural network that can then be used to process data in large volumes.

VI. CONCLUSION

Techniques of electromagnetic inverse scattering theory have been applied to the problem of sea ice remote sensing. Inverse algorithms designed to reconstruct complex permittivity profiles and thickness information on sea ice have been developed and tested in settings ranging from a foam/dry wall slab system in the laboratory to laboratory grown saline ice and Arctic sea ice. The work presented here represents the first concerted, interdisciplinary effort aimed specifically at the problem of reconstructing sea ice physical parameters from scattered electromagnetic field data. For example, sea ice thickness has been a long sought after parameter. The present work establishes a foundation upon which practical methods of large-scale inversion for sea ice thickness, at least for the important case of thin ice, may well be based, as well as directions for further inquiry.

One of the byproducts of a focused effort on such a technologically challenging problem as remotely reconstructing the physical characteristics of a complex random medium, is advances in the mathematical theories underlying the problem. Our work on the sea ice inverse problem has led to fundamental advances in the application of layer-stripping techniques

(a)   (b)
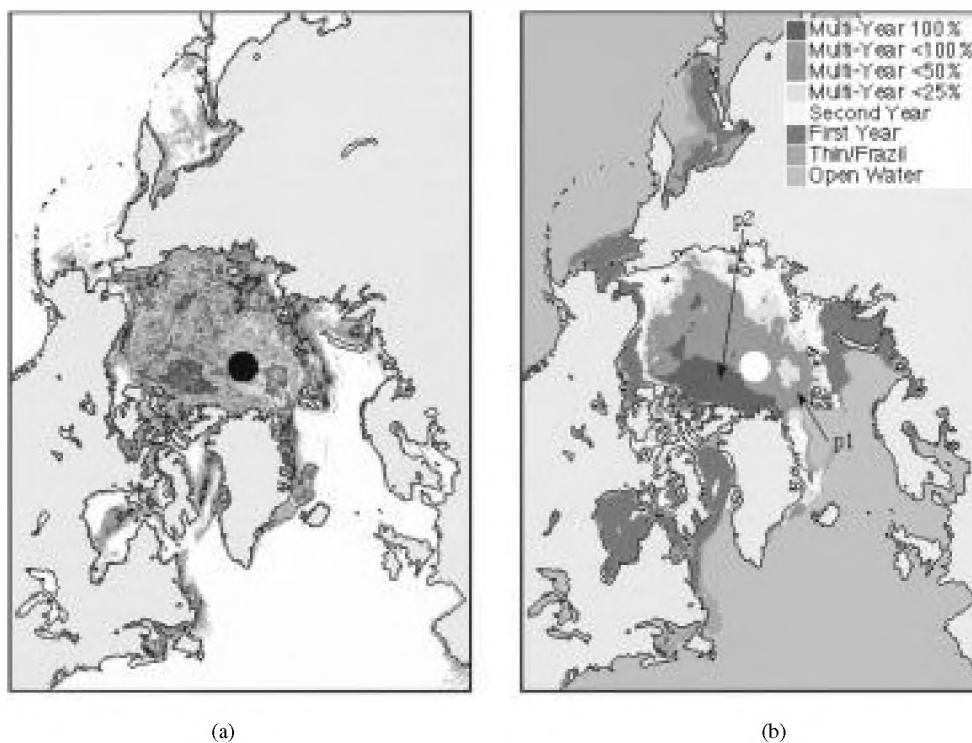
Fig. 17. Qualitative comparison of (a) multiyear ice concentrations with (b) ice age classification results from fast-learning + backpropagation neural network. Based on seven radiometric channels from SSM/I for March 1–15, 1988.

to inverse scattering problems. A new causality method of stabilizing solutions, which is a principal challenge in inverse problems, has been developed. This type of approach has led to a surprising nonlinear generalization of Fourier analysis, which is quite significant mathematically in its own right. Furthermore, rigorously addressing the composite nature of sea ice in this context has led to new developments in the theory of effective parameters of composite media and, in particular, to a theory of inverse homogenization for recovering microstructural features from bulk electromagnetic measurements.

Finally, it should be noted that there still remains much work in refining the algorithms and theoretical results developed here into practical, accurate techniques for reconstructing sea parameters from satellite data. Nevertheless, the present work does take a step in that direction, and we hope that others will be motivated to build upon it.

REFERENCES

[1] S. F. Ackley, V. I. Lytle, K. M. Golden, M. N. Darling, and G. A. Kuehn, "Sea ice measurements during ANZFLUX," *Antarct. J. U.S.*, vol. 30, pp. 133–135, 1995.

[2] S. A. Arcone, A. J. Gow, and S. McGrew, "Structure and dielectric properties at 4.8 and 9.5 GHz of saline ice," *J. Geophys. Res.*, vol. 91, no. C12, pp. 14 281–14 303, 1986.

[3] S. G. Beaven, G. L. Lockhart, S. P. Gogineni, K. C. Jezek, A. R. Hosseinmostafa, A. J. Gow, D. K. Perovich, A. K. Fung, and S. Tjuatja, "Laboratory measurements of radar backscatter from bare and snow-covered saline ice sheets," *Int. J. Remote Sensing*, vol. 16, pp. 851–876, 1995.

[4] D. J. Bergman, "The dielectric constant of a composite material—A problem in classical physics," *Phys. Rep. C*, vol. 43, pp. 377–407, 1978.

[5] ———, "Rigorous bounds for the complex dielectric constant of a two—Component composite," *Ann. Phys.*, vol. 138, p. 78, 1982.

[6] M. Born, "Quantenmechanik der sto vargänger," *Z. Physik*, vol. 38, pp. 803–827, 1926.

[7] O. Bruno, "The effective conductivity of strongly heterogeneous composites," in *Proc. R. Soc. Lond. A*, 1991, vol. 433, pp. 353–381.

[8] F. D. Carsey, R. G. Barry, D. A. Rothrock, and W. F. Weeks, "Status and future directions for sea ice remote sensing," in *Microwave Remote Sensing of Sea Ice, Geophysical Monograph 68*, F. D. Carsey, Ed. Washington, DC: Amer. Geophys. Union, 1992, pp. 443–446.

[9] H. S. Carslaw and J. C. Jaeger. *Conduction of Heat in Solids*. London, U.K.: Oxford Univ. Press, 1959.

[10] D. J. Cavalieri, J. P. Crawford, M. R. Drinkwater, D. T. Eppler, L. D. Farmer, R. R. Jentz, and C. C. Wackman, "Aircraft active and passive microwave validation of sea ice concentration from the defense meteorological satellite program special sensor microwave imager," *J. Geophys. Res.*, vol. 96, no. C12, pp. 21 989–22 008, 1991.

[11] B. J. Chaderjian, "Determination of a stratified acoustic medium with attenuation from its response to a point source," Ph.D. dissertation, Univ. California, Los Angeles, 1989.

[12] ———, "A uniqueness theorem for a lossy inverse problem in reflection seismology," *SIAM J. Appl. Math.*, vol. 54, pp. 1224–1249, 1989.

[13] G. Chavent and P. C. Sabatier, Eds., *Inverse Problems of Wave Propagation and Diffraction, Lecture Notes in Physics*, vol. 486. New York: Springer-Verlag, 1997.

[14] Y. Chen and V. Rokhlin, "On the inverse scattering problem for the Helmholtz equation in one dimension," *Inv. Prob.*, vol. 8, pp. 365–390, 1992.

[15] M. Cheney, "Stability analysis of the Yagle–Levy multidimensional inverse scattering algorithm," *J. Math. Phys.*, vol. 31, pp. 2141–2144, 1990.

[16] M. Cheney and D. Isaacson, "Inverse problems for a perturbed dissipative half-space," *Inv. Prob.*, vol. 11, pp. 865–888, 1995.

[17] M. Cheney, D. Isaacson, V. I. Lytle, and S. F. Ackley, "Recovery of surface parameters from stepped-frequency radar returns," submitted for

publication.

[18] E. Cherkaeva, "On uniqueness of recovering the microstructure of a composite from effective property measurements," submitted for publication.

[19] E. Cherkaeva and K. M. Golden, "Inverse bounds on the brine volume of sea ice derived from complex permittivity data," submitted for publication.

[20] E. Cherkaeva and A. C. Tripp, "Bounds on porosity for dielectric logging," in *European Consortium for Mathematics in Industry'96.* Lyngby, Denmark: Danish Tech. Univ., 1996, pp. 304–306.

[21] W. C. Chew, *Waves and Fields in Inhomogeneous Media.* New York: IEEE, 1995.

[22] D. Colton and R. Kress, *Inverse Acoustic and Electromagnetic Scattering Theory,* 2nd ed. New York: Springer-Verlag, 1998.

[23] J. Comiso, private communication, 1985.

[24] R. Courant and D. Hilbert, *Methods of Mathematical Physics,* vol. 2. New York: Wiley, 1962.

[25] P. Coutu, "Radiative transfer theory for active remote sensing of sea ice," M.S. thesis, Dept. Elect. Eng. Comput. Sci., Massachusetts Inst. Technol., Cambridge, 1993.

[26] G. F. N. Cox and W. F. Weeks, "Salinity variations in sea ice," *J. Glaciol.,* vol. 13, no. 67, pp. 109–120, 1974.

[27] M. S. Dawson, A. K. Fung, and M. T. Manry, "Sea ice classification using fast learning neural networks," in *Proc. IEEE IGARSS'92 Symp.,* p. 1070.

[28] _____, "Robust statistical-based estimator for soil moisture retrieval from radar measurements," *IEEE Trans. Geosci. Remote Sensing,* vol. 35, pp. 57–67, Jan. 1997.

[29] M. R. Drinkwater and G. B. Crocker, "Modeling changes in the dielectric and scattering properties of young snow-covered sea ice at GHz frequencies," *J. Glaciol.,* vol. 34, pp. 274–282, 1988.

[30] M. R. Drinkwater, R. Kwok, and D. P. Winebrenner, "Multi-frequency polarimetric SAR observations of sea ice," *J. Geophys. Res.,* vol. 96, no. C11, pp. 20 679–20 698, 1991.

[31] H. Engl, A. Louis, and W. Rundell, *Inverse Problems in Geophysical Applications.* Philadelphia, PA: Soc. Ind. Appl. Math., 1997.

[32] D. T. Eppler, L. D. Farmer, A. W. Lohanick, and M. Hoover, "Classification of sea ice types with single band (33.6 GHz) airborne passive microwave imagery," *J. Geophys. Res.,* vol. 91, no. C9, pp. 10 661–10 695, 1986.

[33] C. H. Fritsen, V. I. Lytle, S. F. Ackley, and C. W. Sullivan, "Autumn bloom of Antarctic pack-ice algae," *Science,* vol. 266, pp. 782–784, 1994.

[34] A. K. Fung, *Microwave Scattering and Emission Models and Their Applications.* Norwood, MA: Artech House, 1994.

[35] A. K. Fung and R. G. Onstott, "Modeling of ice thickness effect and its application to data interpretation," in *Proc. IEEE IGARSS'96 Symp.,* pp. 1202–1204.

[36] K. M. Golden, "Bounds on the complex permittivity of sea ice," *J. Geophys. Res.,* vol. 100, no. C7, pp. 13 699–13 711, 1995.

[37] K. M. Golden and G. Papanicolaou, "Bounds for effective parameters of heterogeneous media by analytic continuation," *Commun. Math. Phys.,* vol. 90, pp. 473–491, 1983.

[38] K. M. Golden, "Critical behavior of transport in percolation-controlled smart composites," in *SPIE Proc. Math. Contr. Smart Structures,* V. V. Varadan and J. Chandra, Eds. Bellingham, WA: SPIE, 1997, vol. 3039, pp. 571–581.

[39] _____, "The interaction of microwaves with sea ice," in *Wave Propagation in Complex Media, IMA Volumes in Mathematics and Its Applications,* vol. 96, G. Papanicolaou, Ed. Berlin, Germany: Springer-Verlag, 1997, pp. 75–94.

[40] K. M. Golden, S. F. Ackley, and V. I. Lytle, "Brine percolation in sea ice," submitted for publication.

[41] K. M. Golden, M. Cheney, K.-H. Ding, A. K. Fung, T. C. Grenfell, D. Isaacson, J. A. Kong, S. V. Nghiem, J. Sylvester, and D. P. Winebrenner, "Forward electromagnetic scattering models for sea ice," this issue, pp. 1655–1674.

[42] T. C. Grenfell, D. G. Barber, A. K. Fung, A. J. Gow, K. C. Jezek, E. J. Knapp, S. V. Nghiem, R. G. Onstott, D. K. Perovich, C. S. Roesler, C. T. Swift, and F. Tanis, "Evolution of electromagnetic signatures of sea ice from initial formation to the establishment of thick first-year ice," this issue, pp. 1642–1654.

[43] T. C. Grenfell, D. J. Cavalieri, J. C. Comiso, M. R. Drinkwater, R. G. Onstott, I. Rubinstein, K. Steffen, and D. P. Winebrenner, "Considerations for microwave remote sensing of thin sea ice," in *Microwave Remote Sensing of Sea Ice, Geophysical Monograph 68,* F. D. Carsey, Ed. Washington, DC: Amer. Geophys. Union, 1992, pp. 291–301.

[44] J. E. Groves and W. J. Stringer, "The use of AVHRR thermal infrared imagery to determine sea ice thickness within the Chukchi polynya," *Arctic,* vol. 44, no. (supplement 1), pp. 130–139, 1991.

[45] J. Hadamard, *Lectures on the Cauchy Problem in Linear Partial Differential Equations.* New Haven, CT: Yale Univ. Press, 1923.

[46] M. Hallikainen, "Microwave remote sensing of low-salinity sea ice," in *Microwave Remote Sensing of Sea Ice, Geophysical Monograph 68,* F. D. Carsey, Ed. Washington, DC: Amer. Geophys. Union, 1992, pp. 361–373.

[47] J. Hollinger, R. Lo, G. Poe, R. Savage, and J. Peirce, "Special sensor microwave/imager use/guide," Naval Res. Lab., Washington, DC, 1987.

[48] K. I. Hopcraft and P. R. Smith, *An Introduction to Electromagnetic Inverse Scattering.* Dordrecht, Germany: Kluwer, 1992.

[49] D. D. Huynh, S. H. Yueh, S. V. Nghiem, and R. Kwok, "Neural networks and its applications to polarimetric remote sensing," Jet Propul. Lab., Pasadena, CA, Tech. Rep., Sept. 1992.

[50] D. Isaacson, J. C. Newell, J. C. Goble, and M. Cheney, "Thoracic impedance images during ventilation," in *Proc. IEEE-EMBS Conf 12,* 1990.

[51] A. Ishimaru, R. J. Marks II, L. Tsang, C. M. Lam, and D. C. Park, "Particle size distribution determination using optical sensing and neural networks," *Opt. Lett.,* vol. 15, pp. 1221–1223, 1990.

[52] A. K. Jordan and M. E. Veysoglu, "Electromagnetic remote sensing of sea ice," *Inv. Prob.,* vol. 10, no. 5, pp. 1041–1058, 1994.

[53] C. M. Adams Jr., D. N. French, and W. D. Kingery, "Solidification of sea ice," *J. Glaciol.,* vol. 3, no. 28, pp. 745–761, 1960.

[54] A. Kirsch, *An Introduction to the Mathematical Theory of Inverse Problems.* New York: Springer-Verlag, 1996.

[55] J. A. Kong, *Electromagnetic Wave Theory,* 2nd ed. New York: Wiley, 1990.

[56] G. Kristensson and R. J. Krueger, "Direct and inverse scattering in the time domain for a dissipative wave equation, part 4: Use of phase velocity mismatches to simplify inversions," *Inv. Prob.,* vol. 5, pp. 375–388, 1989.

[57] L. Kurvonen and M. Hallikainen, "Classification of Baltic sea ice types by airborne multifrequency microwave radiometer. *IEEE Trans. Geosci. Remote Sensing,* vol. 34, pp. 1292–1299, Nov. 1996.

[58] R. Kwok, S. V. Nghiem, S. H. Yueh, and D. D. Huynh, "Retrieval of thin ice thickness from multifrequency polarimetric SAR data," *Remote Sens. Environ.,* vol. 51, pp. 461–474, 1995.

[59] R. Kwok, E. Rignot, B. Holt, and R. G. Onstott, "Identification of sea ice types in spaceborne synthetic aperture radar data," *J. Geophys. Res.,* vol. 97, no. C2, pp. 2391–2402, 1992.

[60] R. P. Lippmann, "Introduction to computing with neural nets," *IEEE Trans. Acoust., Speech, Signal Processing,* vol. ASSP-, pp. 4–22, Jan. 1987.

[61] V. I. Lytle and S. F. Ackley, "Permittivity of sea ice at Ka-band," in *Proc. IEEE IGARSS'95 Symp.,* pp. 410–413.

[62] _____, "Heat flux through sea ice in the Western Weddell Sea: Convective and conductive transfer processes," *J. Geophys. Res.,* vol. 101, no. C4, pp. 8853–8868, 1996.

[63] M. T. Manry, M. S. Dawson, A. K. Fung, S. Apollo, L. Allen, and W. Lyleand, W. Gong, "Fast training of neural networks for remote sensing," *Remote Sens. Rev.,* vol. 9, pp. 77–96, 1994.

[64] N. J. Marechal, "Inverse problems for lossy hyperbolic equations," Ph.D. dissertation, Univ. California, Los Angeles, 1989.

[65] D. W. Marquardt, "An algorithm for least-squares estimation of nonlinear parameters," *J. Soc. Indust. Appl. Math.,* vol. 11, pp. 431–441, 1963.

[66] R. Massom and J. C. Comiso, "The classification of Arctic sea ice types and the determination of surface temperature using advanced very high resolution radiometer data," *J. Geophys. Res.,* vol. 99, pp. 5201–5218, 1994.

[67] G. A. Maykut, "Energy exchange over young sea ice in the central Arctic," *J. Geophys. Res.,* vol. 83, no. C7, 1978.

[68] _____, "The surface heat and mass balance," in *The Geophysics of Sea Ice,* N. Untersteiner, Ed. New York: Plenum, 1986, pp. 395–463.

[69] R. C. McPhedran, D. R. McKenzie, and G. W. Milton, "Extraction of structural information from measured transport properties of composites," *Appl. Phys. A,* vol. 29, pp. 19–27, 1982.

[70] R. C. McPhedran and G. W. Milton, "Inverse transport problems for composite media," *Mat. Res. Soc. Symp. Proc.,* 1990, vol. 195, pp. 257–274.

[71] G. Muller, "The reflectivity method: A tutorial," *J. Geophys.,* vol. 58, pp. 153–174, 1985.

[72] S. V. Nghiem, R. Kwok, S. H. Yueh, and M. R. Drinkwater, "Polarimetric signatures of sea ice 1. Theoretical model," *J. Geophys. Res.,* vol. 100, no. C7, pp. 13 665–13 679, 1995.

[73] S. V. Nghiem, R. Kwok, S. H. Yueh, A. J. Gow, D. K. Perovich, J. A. Kong, and C.-C. Hsu, "Evolution in polarimetric signatures of thin saline ice under constant growth," *Radio Sci.*, vol. 32, pp. 127–151, 1997.

[74] M. O'Donnell, E. T. Jaynes, and J. G. Miller, "Kramers–Kronig relationship between ultrasonic attenuation and phase velocity," *JASA*, vol. 69, no. 3, 1981.

[75] J. A. Ogilvy, *Theory of Wave Scattering from Random Rough Surfaces*. London, U.K.: IOP, 1991.

[76] A. V. Oppenheim and R. W. Schafer, *Digital Signal Processing*. Englewood Cliffs, NJ: Prentice-Hall, 1975.

[77] C. Orum, E. Cherkaeva, and K. M. Golden, "Recovery of inclusion separations in a composite from effective property measurements," submitted for publication.

[78] L. Päivärinta and E. Somersalo, *Inverse Problems in Mathematical Physics, Springer Lecture Notes in Physics*, vol. 422. Berlin, Germany: Springer-Verlag, 1992.

[79] Y. H. Pao, *Adaptive Pattern Recognition and Neural Networks*. Reading, MA: Addison-Wesley, 1989.

[80] J. L. Peirce, Ed., *Special Sensor Microwave/Imager Critical Design Review*, Hughes Aircraft Co., Space Segment, Contract F04701-79-C-0061, 1980, vol. 1.

[81] E. Polack and G. Ribiere, "Notes sur la convergence de méthodes de diréctions conjugées, *Revue Fr. Inf Rech. Oper.*, vol. 16, no. R1, pp. 35–43, 1969.

[82] R. L. Rennie, "Dielectric measurement of sea ice in the frequency range 26.5 to 40 GHz using a quasioptical technique," M.S. thesis, Dartmouth College, Hanover, NH, 1991.

[83] D. E. Rumelhart and J. L. McClelland, Eds., *Parallel Distributed Processing*, vols. 1–2. Cambridge, MA: MIT Press, 1986.

[84] E. Rutheford, "The scattering of α and β particles by matter and the structure of the atom," *Phil. Mag. 6th Ser.*, vol. 21, pp. 669–688, 1911.

[85] R. Sawicz and K. M. Golden, "Bounds on the complex permittivity of matrix-particle composites," *J. Appl. Phys.*, vol. 78, pp. 7240–7246, 1995.

[86] S.-E. Shih, K.-H. Ding, S. V. Nghiem, C.-C. Hsu, J. A. Kong, and A. K. Jordan, "Saline ice thickness retrieval using time series C-band polarimetric radar measurements," this issue, pp. 1731–1742.

[87] ——, "Thickness retrieval using time series electromagnetic measurements of laboratory grown saline ice," in *Proc. IEEE IGARSS'96 Symp.*, 1996, pp. 1208–1210.

[88] E. Somersalo, M. Cheney, D. Isaacson, and E. Isaacson, "Layer stripping: A direct numerical method for impedance imaging," *Inv. Prob.*, vol. 7, pp. 899–926, 1991.

[89] K. St. Germain, C. T. Swift, and T. C. Grenfell, "Determination of dielectric constant of young sea ice using microwave spectral radiometry," *J. Geophys. Res.*, vol. 98, pp. 4675–4679, 1993.

[90] K. Steffen and J. A. Maslanik, "Comparison of Nimbus 7 SMMR radiance and derived sea ice concentrations with Landsat imagery from the North Water area of Baffin Bay," *J. Geophys. Res.*, vol. 93, pp. 10 769–10 781, 1988.

[91] C. T. Swift, K. St. Germain, K. C. Jezek, S. P. Gogineni, A. J. Gow, D. K. Perovich, T. C. Grenfell, and R. G. Onstott, "Laboratory investigations of the electromagnetic properties of artificial sea ice," in *Microwave Remote Sensing of Sea Ice, Geophysical Monograph 68*, F. D. Carsey, Ed. Washington, DC: Amer. Geophys. Union, 1992, pp. 443–446.

[92] J. Sylvester and G. Uhlmann, "A global uniqueness theorem for an inverse boundary value problem in electrical prospection," *Ann. Math.*, vol. 125, pp. 153–169, 1987.

[93] J. Sylvester and D. Winebrenner, "Linear and nonlinear inverse scattering," *SIAM J. Appl. Math*, to be published.

[94] J. Sylvester, D. Winebrenner, and F. Gylys-Colwell, "Layer stripping for the Helmholtz equation," *SIAM J. Appl. Math.*, vol. 56, pp. 736–754, 1996.

[95] A. C. Tripp, E. Cherkaeva, and J. Hulen, "Bounds on the complex conductivity of geophysical mixtures," *Geophysical Prospecting*, to be published.

[96] L. Tsang, Z. Chen, S. Oh, R. J. Marks II, and A. T. C. Chang, "Inversion of snow parameters for passive microwave remote sensing measurements by a neural network trained with a multiple scattering model," in *Proc, Int. Geosci. Remote Sensing Symp.*, Espoo, Finland, 1990, pp. 1965–1966.

[97] L. Tsang, J. A. Kong, and R. T. Shin, *Theory of Microwave Remote Sensing*. New York: Wiley, 1985.

[98] F. T. Ulaby, R. K. Moore, and A. K. Fung, *Microwave Remote Sensing: Active and Passive*, vols. I–III. Reading, MA: Addison-Wesley, 1982.

[99] M. E. Veysoglu, "Direct and inverse scattering models for random media and rough surfaces," Ph.D. dissertation, Dept. Elect. Eng. Comput. Sci., Massachusetts Inst. Technol., 1994.

[100] M. E. Veysoglu, H. T. Ewe, A. K. Jordan, R. T. Shin, and J. A. Kong, "Inversion algorithms for remote sensing of sea ice," in *Proc. IEEE IGARSS'94 Symp.*, pp. 626–628.

[101] R. H. Wade and W. F. Weeks, "Radar backscatter estimates from a surface scattering model of first year sea ice," in *EARSeL Advances in Remote Sensing*, vol. 3. Paris, France: Eur. Assoc. Remote Sensing Lab., 1994, pp. 24–30.

[102] P. Wadhams and J. C. Comiso, "The ice thickness distribution inferred using remote sensing techniques," in *Microwave Remote Sensing of Sea Ice, Geophysical Monograph 68*, F. D. Carsey, Ed. Washington, DC: Amer. Geophys. Union, 1992, pp. 375–383.

[103] P. Wadhams, N. R. Davis, J. C. Comiso, R. Kutz, J. Crawford, G. Jackson, W. Krabill, C. B. Sear, R. Swift, and W. B. Tucker III, "Concurrent remote sensing of Arctic sea ice from submarine and aircraft," *Int. J. Remote Sensing*, vol. 12, pp. 1829–1840, 1991.

[104] W. F. Weeks and S. F. Ackley, "The growth, structure and properties of sea ice," CRREL Mono. 82-1, 1982, p. 130.

[105] A. Weideman, "Computing the Hilbert transform on the real line," *Math. Comput.*, vol. 64, 1995.

[106] T. Wen, W. J. Felton, J. C. Luby, W. L. J. Fox, and K. L. Kientz, "Environmental measurements in the Beaufort Sea," Appl. Phys. Lab., Univ. Washington, Seattle, Tech. Rep., APL-UW TR 8822, 1989.

[107] D. P. Winebrenner, J. Bredow, A. K. Fung, M. R. Drinkwater, S. V. Nghiem, A. J. Gow, D. K. Perovich, T. C. Grenfell, H. C. Han, J. A. Kong, J. K. Lee, S. Mudaliar, R. G. Onstott, L. Tsang, and R. D. West, "Microwave sea ice signature modeling," in *Microwave Remote Sensing of Sea Ice, Geophysical Monograph 68*, F. D. Carsey, Ed. Washington, DC: Amer. Geophys. Union, 1992, pp. 137–175.

[108] D. P. Winebrenner, L. D. Farmer, and I. R. Joughin, "On the response of polarimetric synthetic aperture radar signatures at 24-cm wavelength to sea ice thickness in Arctic leads," *Radio Sci.*, vol. 30, pp. 373–402, 1995.

[109] D. P. Winebrenner and J. Sylvester, "Causally stabilized layer-stripping with bandlimited and noisy data," submitted for publication.

[110] ——, "Inversion of wideband microwave reflectivity to estimate the thickness of Arctic lead-like sea ice," in *Proc. IEEE IGARSS'96 Symp.*, pp. 1205–1207.

[111] A. Yagle and B. Levy, "Layer stripping solutions of multidimensional inverse scattering problems," *J. Math. Phys.*, vol. 27, pp. 1701–1720, 1986.

[112] Y. Yu and D. A. Rothrock, "Thin ice thickness from satellite thermal imagery," *J. Geophys. Res*, vol. 101, no. 25, pp. 753–766, 1996.

[113] I. H. H. Zabel, K. C. Jezek, S. P. Gogineni, and P. Kanagaratnam, "Search for proxy indicators of young sea ice thickness," *J. Geophys. Res.*, vol. 101, pp. 6697–6709, 1996.

K. M. Golden, photograph and biography not available at the time of publication.

D. Borup (M'98), photograph and biography not available at the time of publication.

M. Cheney, photograph and biography not available at the time of publication.

E. Cherkaeva, photograph and biography not available at the time of publication.

M. S. Dawson (S'89–M'90), photograph and biography not available at the time of publication.

Kung-Hau Ding, for a biography, see p. 124 of the January 1998 issue of this TRANSACTIONS.

A. K. Fung (S'60–M'66–SM'70–F'85), photograph and biography not available at the time of publication.

D. Isaacson (M'86), photograph and biography not available at the time of publication.

S. A. Johnson, photograph and biography not available at the time of publication.

Arthur K. Jordan (M'59–SM'74–F'91–LF'96), for a photograph and biography, see this issue, p. 1631.

Jin Au Kong (S'65–M'69–SM'74–F'85), for a photograph and biography, see p. 83 of the January 1998 issue of this TRANSACTIONS.

Ronald Kwok (S'82–M'84), for a photograph and biography, see p. 37 of the January 1998 issue of this TRANSACTIONS.

Son V. Nghiem (M'86), for a photograph and biography, see p. 123 of the January 1998 issue of this TRANSACTIONS.

Robert G. Onstott (S'73–M'79), photograph and biography not available at the time of publication.

J. Sylvester, photograph and biography not available at the time of publication.

D. P. Winebrenner (S'79–M'79–SM'90), photograph and biography not available at the time of publication.

I. H. H. Zabel, photograph and biography not available at the time of publication.